ice | proceedings

Proceedings of the Institution of Civil Engineers
Pages 1–22

Keywords: Computational mechanics, Geotechnical engineering, Stress analysis

A reformulated hardening soil model

T.A. Bower PhD, MEng, AFHEA
Software Engineer; LUSAS, Forge House, 66 High Street, Kingston Upon Thames, KT1 1HN, UK
0000-0002-0982-0895
A.D. Jefferson PhD, MSc, BSc, CEng, MIStructE
Professor; School of Engineering, Cardiff University, Queen's Buildings, The Parade, Cardiff, CF24 3AA, UK
0000-0002-2050-2521

P.J. Cleall PhD, BEng
Reader; School of Engineering, Cardiff University, Queen's Buildings, The Parade, Cardiff, CF24 3AA, UK
0000-0002-4005-5319

The hardening soil (HS) model is an advanced soil plasticity model which incorporates many features including stiffness stress dependency, hardening from initial loading, and soil dilatancy. In this paper, the HS model is explored in depth, and two improvements are proposed. The first is a new shear yield surface and hardening rule that have been reformulated to remove singularities. The second is a robust implicit return mapping scheme. Options for improving the global convergence of finite element analyses are also explored. Single elements tests replicate results from experimental triaxial data and previous versions of the HS model very closely, and at excellent convergence rates. In addition, a slope stability analysis is performed using the φ-c strength reduction method in 2D plane-strain. Results from the slope analysis showed good agreement with analytical and graphical slope stability methods. A 3D slope stability analysis was also conducted with modified boundary conditions, in order to demonstrate the 3D capabilities of the model.

Notation

α	Cap shape parameter
γ	Shear strain
γ_p	Plastic shear strain
$\boldsymbol{\Delta\varepsilon}$	Strain increment vector
$\delta\lambda$	Variation in plasticity multiplier
$\Delta\lambda$	Plasticity multiplier
ΔE	Change in Young modulus between iterations
$\boldsymbol{\varepsilon}$	Strain vector
$\boldsymbol{\varepsilon^p}$	Plastic strain vector
ε_v	Volumetric strain
ε_v^p	Plastic volumetric strain
θ	Lode angle
ρ	Density
$\boldsymbol{\sigma}$	Stress vector
$\boldsymbol{\sigma_{LC}}$	Last converged stress
σ^{ref}	Reference stress
$\boldsymbol{\sigma_{tr}}$	Trial stress
φ	Friction angle
φ_c	Critical state friction angle
φ_m	Mobilised friction angle
χ	Cap shaping parameter
ψ	Dilatancy angle
ψ_m	Mobilised dilatancy angle
c	Cohesion
$\boldsymbol{D_e}$	Elastic stiffness matrix
$\boldsymbol{D_{ep}}$	Pseudo-consistent tangent matrix
E_{ur}^{ref}	Reference unload-reload modulus
E_i^{ref}	Reference initial modulus
m	Stiffness stress dependency exponent
p	Mean stress
p_p	Pre-consolidation pressure
q_a	Asymptotic shear stress
q_f	Failure shear stress

1. Introduction

The hardening soil (HS) model is a soil plasticity model which is gaining increasing popularity in research and design and has been implemented into commercial finite element codes such as Plaxis (PLAXIS, 2016), ZSoil (Obrzud, 2010), and FLAC^{3D} (Jiang and Zhang, 2012). This a multiple surface plasticity model which combines many advanced features such as stress-dependent stiffness, non-linear dilatancy progression, and separate mechanisms for controlling the shear and the volumetric behaviour of the soil.

The parameters used in the model are easily obtainable from standard soil laboratory tests. To date, several versions of the model have been created; the model was first proposed by Schanz et al. (1999). This version makes use of a hexagonal Mohr-Coulomb type cone surface which hardens according to a rule based on the hyperbolic soil model (Duncan and Chang, 1970) It also features an

elliptical cap surface, similar to that used in the Modified Cam-Clay model (Roscoe and Burland, 1968).

Modifications to this model were proposed by Benz (2007) and Benz et al. (2008), which addressed the non-smooth failure criterion used in the model, citing that the new failure criterion better captures the experimental failure criterion observed in soils (Matsuoka and Nakai, 1974). This improvement is explained by the contribution of the intermediate principal stress to failure. Another part of the work by Benz (2007) was the introduction of a small-strain stiffness overlay to the HS model. Although this small-strain stiffness phenomenon is typically observed in dynamic problems, it was shown that it can improve the results of large boundary-value static problems.

Marcher and Vermeer (2001) introduced softening in the HS model by implementing a void ratio-dependent friction angle. Another modification was made by Truty and Obrzud (2015), which studied the predictions of undrained behaviour in the HS model.

This paper describes the development of a new version of the HS model, hereinafter referred to as the HS-LC model (LUSAS-Cardiff University). The innovations in the new version of the model include a modified shear yield criterion, which in the HS-LC model, is based on the smooth failure criterion by Matsuoka and Nakai (Matsuoka and Nakai, 1974; Panteghini and Lagioia, 2013). The size of the shear cone is controlled by a new hardening rule, which is based on the triaxial shear hyperbola by Duncan and Chang (1970). A robust return mapping procedure is also implemented, which reduces the residuals of stress, plastic strain, and the hardening variables. This model is then verified against previous versions of the HS model, against published experimental data, and a slope stability analysis is performed.

2. Conventions

This paper follows the sign convention of general solid mechanics, where tensile stresses and strains are taken as positive. The principal stresses are ordered descending $\sigma_1 \geq \sigma_2 \geq \sigma_3$. Vectors and matrices are denoted in bold. The unique terms of the three-dimensional stress tensor are represented in the vector:

$$\boldsymbol{\sigma} = \begin{bmatrix} \sigma_x & \sigma_y & \sigma_z & \sigma_{xy} & \sigma_{yz} & \sigma_{xz} \end{bmatrix}^T \tag{1}$$

and similarly for the strain tensor $\boldsymbol{\varepsilon}$. Several stress invariants are used throughout this paper to describe the HS and HS-LC models. The mean stress is calculated from the normal stress components.

$$p = \frac{\sigma_x + \sigma_y + \sigma_z}{3} \tag{2}$$

The shear stress is defined as

$$q = \sqrt{\frac{(\sigma_x - \sigma_y)^2 + (\sigma_y - \sigma_z)^2 + (\sigma_z - \sigma_x)^2}{2} + 3\left(\sigma_{xy}^2 + \sigma_{yz}^2 + \sigma_{xz}^2\right)} \tag{3}$$

The third deviatoric stress invariant is the determinant of the deviatoric stress tensor

$$\begin{aligned} J_3 = (\sigma_x - p)\left[(\sigma_y - p)(\sigma_z - p) - \sigma_{yz}^2\right] \\ -\sigma_{xy}\left[\sigma_{xy}(\sigma_z - p) - \sigma_{yz}\sigma_{xz}\right] \\ +\sigma_{xz}\left[\sigma_{xy}\sigma_{yz} - (\sigma_y - p)\sigma_{xz}\right] \end{aligned} \tag{4}$$

The Lode angle is calculated from the shear stress and third deviatoric stress invariant

$$\theta = \frac{1}{3}\arcsin\left(\frac{-27J_3}{2q^3}\right) \tag{5}$$

and is equal to $\pi/6$ in triaxial compression ($\sigma_1 = \sigma_2 > \sigma_3$). The volumetric strain is the sum of the normal strains

$$\varepsilon_v = \varepsilon_x + \varepsilon_y + \varepsilon_z \tag{6}$$

The shear strain, as defined by Wood (1990) is given as

$$\gamma = \sqrt{\frac{2}{9}\left[(\varepsilon_x - \varepsilon_y)^2 + (\varepsilon_y - \varepsilon_z)^2 + (\varepsilon_z - \varepsilon_x)^2\right] + \frac{1}{3}\left[\varepsilon_{xy}^2 + \varepsilon_{yz}^2 + \varepsilon_{xz}^2\right]} \tag{7}$$

3. Background to the hardening soil model

The HS model is a non-linear soil plasticity model used for the analysis of granular and cohesive soils, which utilises three main yield surfaces:

- A shear surface which hardens from initial loading
- A cap surface to control volumetric strains
- A Mohr-Coulomb failure envelope to impose a final limit on shear stress

Benz (2007) suggested the replacement of the hexagonal Mohr-Coulomb type yield surface with the smooth variation by Matsuoka and Nakai (1974), which produces the same results as the Mohr-Coulomb surface in triaxial conditions when the Lode angle $\theta = \pm\pi/6$. The main advantages of this smoothed surface are the

consideration of the intermediate principal stress at soil failure, and is more computationally convenient due to a reduction in the number of edges and corners which define the yield surface.

The surfaces in each version were formulated to follow the triaxial hyperbola (Eq. 8) proposed by Duncan and Chang (1970) (Figure 1).

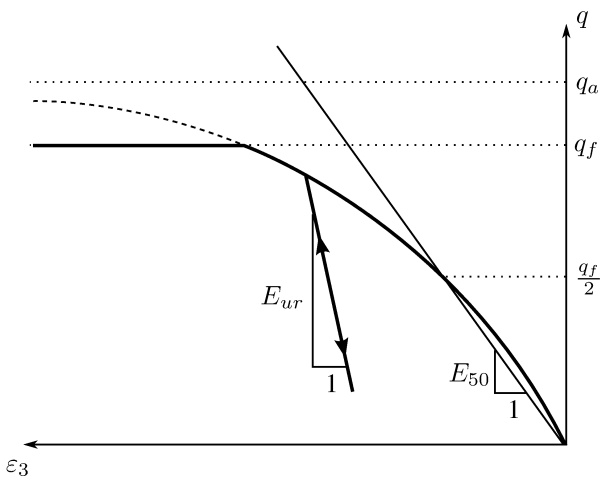

Figure 1. Triaxial compression shearing hyperbola as used in the formulation of HS model, redrawn from Benz (2007).

The equation of the hyperbola in Figure 1 is given by

$$\varepsilon_3 = \frac{q_a}{2E_{50}} \frac{q}{q - q_a} \tag{8}$$

The shear stress q is limited to the failure shear stress q_f (given by the Mohr-Coulomb criterion)

$$q_f = \frac{2\sin\varphi}{1-\sin\varphi}\left(-\sigma_1 + c\cot\varphi\right) \tag{9}$$

where c is the effective cohesion, and φ is the friction angle at failure. E_{50} is the secant stiffness at 50% mobilised shear stress (see Figure 1). The asymptotic shear stress q_a is given by

$$q_a = \frac{q_f}{R_f} \tag{10}$$

where R_f is the failure ratio, which describes the ratio of the failure shear stress to the asymptotic shear stress. A set of stress-dependent stiffness parameters are used throughout the model. These are based on a reference stress σ^{ref} and a stiffness stress dependency exponent m.

$$E_{ur} = E_{ur}^{ref}\left(\frac{-\sigma_1 + c\cot\varphi}{-\sigma^{ref} + c\cot\varphi}\right)^m \tag{11}$$

$$E_{50} = E_{50}^{ref}\left(\frac{-\sigma_1 + c\cot\varphi}{-\sigma^{ref} + c\cot\varphi}\right)^m \tag{12}$$

E_{ur}^{ref} and E_{50}^{ref} are the reference moduli for unloading/reloading and 50% failure shear stress respectively, these are the given values at σ^{ref}. It is worth noting that a constant stiffness can be achieved by setting $m = 0$.

The dilatancy angle ψ_m is also dependent on stress in the HS model; this is used in the plastic potential function to define the gradients of stress return to the shear yield surface. Schanz et al. (1999) used Rowe's stress dilatancy theory (Eq. 13) (Rowe, 1962), and Benz (2007) suggested other alternatives (Søreide, 1990; Li and Dafalias, 2000; Wehnert, 2006).

$$\sin\psi_m = max\left(0, \frac{\sin\varphi_m - \sin\varphi_c}{1 - \sin\varphi_m \sin\varphi_c}\right) \tag{13}$$

The critical state friction angle φ_c is given by

$$\sin\varphi_c = \frac{\sin\varphi - \sin\psi}{1 - \sin\varphi\sin\psi} \tag{14}$$

Additionally, the mobilised friction angle φ_m when using the Mohr-Coulomb model is

$$\sin\varphi_m = \frac{\sigma_1 - \sigma_3}{2c\cot\varphi - \sigma_1 - \sigma_3} \tag{15}$$

Benz (2007) used an alternative definition of the mobilised friction angle to match the Matsuoka-Nakai criterion (Matsuoka and Nakai, 1974).

The shear surface in the HS model is formulated by first taking a position on the hyperbola defined in Eq. 8, this is the first two fractions of Eq. 16. A full unloading step to $q = 0$ is then subtracted, this is the third fraction. The remainder of this unloading is defined by the accumulated plastic shear strain γ_p, and is used as a hardening parameter for this surface.

$$f_s = \frac{q_a}{2E_{50}} \frac{q}{q_a - q} - \frac{q}{E_{ur}} - \gamma_p = 0 \tag{16}$$

Note that the definition in Eq. 16 is different to those quoted by Schanz et al. (1999) and Benz (2007) due to the different definition of shear strain (Eq. 7). This hardening cone is active until the shear stress q reaches the failure shear stress q_f. It is important to note that the shear yield surface (Eq. 16) continues to harden after the failure shear stress is exceeded whenever the minor principal stress σ_1 increases. Therefore, with the HS model, it is necessary to check for yielding of the hardening shear surface, even if the failure criterion has been exceeded previously.

In the two prior version of the HS model, the failure surface is defined by either the Mohr-Coulomb criterion (Eq. 17) or the Matsuoka-Nakai criterion (Eq. 18).

$$f_{MC} = \frac{\sigma_1 + \sigma_3}{2} \sin\varphi + \frac{\sigma_1 - \sigma_3}{2} + c\cos\varphi = 0 \quad (17)$$

$$f_{MN} = \frac{I_1 I_2}{I_3} - \left(9 + 8\tan^2\varphi\right) = 0 \quad (18)$$

where I_1, I_2 and I_3 are the first, second and third invariants of the stress tensor. The first advantage of using the Matsuoka-Nakai criterion is that the intermediate principal stress is considered; secondly, the smooth yield is more convenient computationally, as fewer corners / edges are present than in the Mohr-Coulomb yield surface.

The plastic potential used with both of the shear yield surfaces is the circular cone presented by Drucker et al. (1952).

$$g_s = q + (p - c\cot\varphi)\,\frac{6\sin\psi_m}{3 - \sin\psi_m} \quad (19)$$

The internal angle of the cone is determined by the mobilised dilatancy angle ψ_m. Alternate shear plastic potential functions may also be implemented with the HS model, as use of different potential functions has been shown to change the model behaviour; in particular the treatment of the Lode angle after failure (Lagioia and Panteghini, 2014).

The cap surface takes the form of an ellipse in p-q space

$$f_c = p^2 + \left(\frac{q}{\chi\alpha}\right)^2 - p_p^2 = 0 \quad (20)$$

The steepness of the cap is controlled using the parameter α, and χ is a Lode angle-dependent variable (defined later in Eq. 35) which varies the shape of the cap surface in the deviatoric plane such that the locus of its intersection with the shear surface lies on the plane

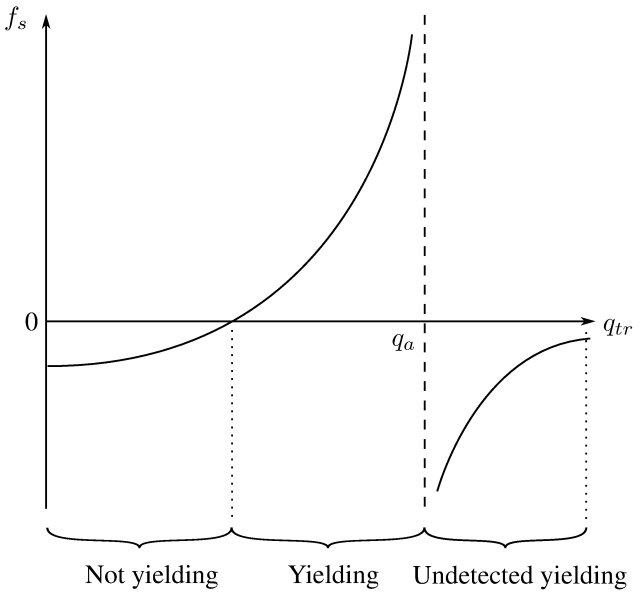

Figure 2. Shear yield function value against shear stress. Yielding is not detected when the trial shear stress q_{tr} exceeds q_a.

perpendicular to the isotropic compression line $\sigma_1 = \sigma_2 = \sigma_3$. The pre-consolidation pressure p_p is used as a hardening parameter and controls the overall size of the cap. The cap surface uses an associated flow rule.

4. Changes to the hardening soil model

There are a number of aspects of the existing HS formulations that can give rise to numerical difficulties. The first issue relates to the form of the shear yield surface (Eq. 16). In many return mapping schemes it is necessary to calculate a 'trial stress', which is obtained by using elastic stiffness for the given strain increment. If the trial shear stress exceeds the asymptotic shear stress, i.e. $q > q_a$, then the yield function would become negative, and the return mapping algorithms could not detect yielding on the shear surface, as illustrated in Figure 2. Additionally, a trial stress of $q = q_a$ creates a division by zero in the shear yield surface. This issue has also been noted by Cocco and Ruiz (2018). To overcome this difficulty, the shear surface has been reformulated so that it remains positive for any shear stress higher than yield, thus allowing implementation of the Hardening Soil model in stress return mapping schemes such as closest point projection (CPP).

The use of a second surface to define failure has also been removed in this reformulation, as the mating of a hardening yield surface with a fixed failure surface was found to create numerical difficulties. Instead, soil failure is incorporated into the hardening function of the reformulated shear yield surface.

The next issue is the incremental form of the shear hardening parameter γ_p as it was found to cause the global Newton-Raphson scheme to converge at an increasingly slower rate throughout load incrementation. It was discovered that this was due to drifting of the solution; the hardening parameter represents the plastic shear strain, and with continued shear strain steps, the hardening parameter would tend to deviate from the plastic strains calculated in the return mapping procedure. This issue is addressed by using the plastic strains directly in the yield function.

Benz (2007) documents use of the CPP method for one and two surface stress returns. However, in this formulation, only the residual for the stresses are reduced during each iteration and the return mapping procedure is based on incremental relationships. In the algorithm presented in this paper, residuals for the plastic strain and the hardening variables are also reduced, leading to algorithm which converges faster. Additionally, the incremental cap hardening residual is taken into account in the new algorithm. The use of a relationship between total rather than incremental terms reduces the tendency for the solution to drift from the governing equations and reduces step size-dependency.

4.1. Shear surface

The following section details the steps taken to reformulate the shear surface in the HS-LC model. In triaxial stress states, the relationship between the axial plastic strain and shear stress is given by Kondner's hyperbola (Eq. 8).

$$\varepsilon_3^p = \frac{q_a}{2E_{50}} \frac{q}{q - q_a} + \frac{q}{E_{ur}} \tag{21}$$

In triaxial stress states ($\theta = \pm\pi/6$), the minor and intermediate principal strains are equal ($\varepsilon_1 = \varepsilon_2$), substituting this relationship into the definition of the shear strain (Eq. 7) gives the triaxial plastic shear strain.

$$\gamma^p = \frac{2}{3}\left(\varepsilon_1 - \varepsilon_3\right) \tag{22}$$

As the hardening of the shear yield function is related solely to plastic shear strain, a state of pure shear is considered; i.e.

$$\varepsilon_v^p = \varepsilon_1^p + \varepsilon_1^p + \varepsilon_3^p = 0 \tag{23}$$

which leads to the relationship

$$\varepsilon_1^p = -\frac{1}{2}\varepsilon_3^p \tag{24}$$

Substituting Eq. 24 into Eq. 22 gives the relation between plastic triaxial shear strain and axial strain.

$$\gamma^p = -\varepsilon_3^p \tag{25}$$

Substituting Eq. 25 back into Eq. 21 gives the relation between the plastic shear strain and hyperbola used in the HS-LC model.

$$0 = \frac{q_a}{2E_{50}} \frac{q}{q_a - q} - \frac{q}{E_{ur}} - \gamma^p \tag{26}$$

In order to obtain a normalised hardening function which has the limits 0 and 1, the function is formulated to equal the ratio of the shear stress and the asymptotic shear stress. Letting $r_q = q/q_a$ and $r_u = E_{ur}/2E_{50}$ and through manipulation of Eq. 26 the following hardening function is obtained:

$$r_q = \frac{1}{2}\sqrt{\left(r_u - 1 + \frac{\gamma^p E_{ur}}{q_a}\right)^2 - \frac{4\gamma^p E_{ur}}{q_a}} - \frac{1}{2}\left(r_u - 1 + \frac{\gamma^p E_{ur}}{q_a}\right) \tag{27}$$

To enforce the shear failure limit at a point below the asymptotic shear stress q_a, the parameter R_f is used as a maximum value, i.e. $r_q \leq R_f$. The hardening function with the imposed upper limit is plotted in Figure 3 for different values of q_a. Intuitively, a higher asymptotic shear stress requires a higher plastic shear strain to reach the failure limit. To maintain stable convergence when $q > q_f$ for standard Newton-Raphson solvers, a very small gradient can be given to the post-failure curve in Figure 3. This gradient is generally only necessary for load-controlled analyses.

The 'loading' and 'failure' surfaces are combined with the latter being the limit of the former. The chosen shear yield function employs Panteghini and Lagioia's reformulated version of the Matsuoka-Nakai failure surface (Panteghini and Lagioia, 2013). The yield function is given by;

$$f_s = q + \frac{M r_q}{\rho R_f}\left(p - c\cot\varphi\right) = 0 \tag{28}$$

in which ρ is the Lode angle-dependent parameter which alters the shape of the yield surface in the π-plane (Eq. 32). M controls the apex angle of the cone (Eq. 33); when $r_q = R_f$, Eq. 28 is equivalent

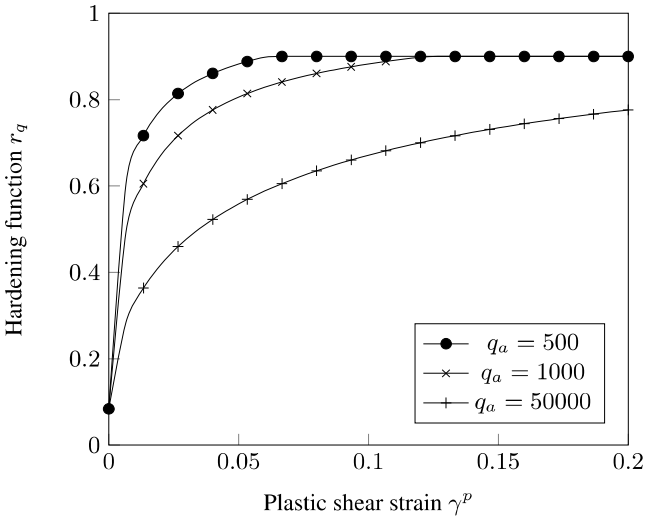

Figure 3. Shear surface hardening function with plastic shear strain with $R_f = 0.9$.

to the Matsuoka-Nakai failure surface (Eq. 18). The definitions of each required intermediate parameter are listed below

$$\eta = \frac{2\sin\varphi}{\sqrt{3+\sin^2\varphi}} \tag{29}$$

$$\xi = \frac{\sin\varphi\left(9-\sin^2\varphi\right)}{\left(3+\sin^2\varphi\right)^{1.5}} \tag{30}$$

The Lode angle dependency is given by

$$\Theta(\theta) = 2\sqrt{3}\cos\left[\frac{1}{3}\arccos\left(\xi\sin(-3\theta)\right)\right] \tag{31}$$

The parameter ρ normalises the Lode angle dependency to triaxial compression. The last converged stress is used in this calculation.

$$\rho = \frac{\Theta(\theta_{LC})}{\Theta(\pi/6)} \tag{32}$$

The parameter M is given by

$$M = \frac{3\sqrt{3}\eta}{\Theta(\pi/6)} \tag{33}$$

This surface uses a non-associated flow rule. The plastic potential is that of Drucker et al. (1952), as described in Eq. 19. The mobilised friction angle is also redefined to match the current failure criterion. This is used in the calculated of the mobilised dilatancy angle $\sin\psi_m$ (Eq. 13).

$$\sin\varphi_m = \frac{3q}{6\chi\left(-p+c\cot\varphi\right)+q} \tag{34}$$

where χ is equivalent to the Lode dependency term described by Schanz et al. (1999) and Benz (2007), and it relates to the terms in this proposed model by the following relationship:

$$\chi = \frac{M}{\rho}\left(\frac{3-\sin\varphi}{6\sin\varphi}\right) \tag{35}$$

The shaping parameter χ is used in the cap yield surface (Eq. 20).

4.2. Tension surface

A tension limit σ_t is imposed on the mean stress in this proposed model as follows;

$$f_t = p - \sigma_t = 0 \tag{36}$$

where σ_t is the tension cutoff and is entered as a material parameter. The tension yield function uses an associated flow rule ($g_t \equiv f_t$) and does not harden.

One of the previous versions of the hardening soil model Benz (2007) made use of a Rankine type criterion to handle tensile stresses. In this formulation, the mean stress criterion is used for computational convenience to minimise the number of edges and corners between the yield surfaces.

5. The closest point projection method

The closest point projection (CPP) method (a type of backward Euler method) is an implicit return mapping scheme (Simo and Hughes, 2006) whereby the returned stress path is based on the gradients at the final converged stress state (Figure 4).

A trial stress $\boldsymbol{\sigma_{tr}}$ is calculated using the elastic stiffness matrix $\boldsymbol{D_e}$, the stress at the last converged state $\boldsymbol{\sigma_{LC}}$ and the total strain increment $\boldsymbol{\Delta\varepsilon}$.

$$\boldsymbol{\sigma_{tr}} = \boldsymbol{\sigma_{LC}} + \boldsymbol{D_e}\boldsymbol{\Delta\varepsilon} \tag{37}$$

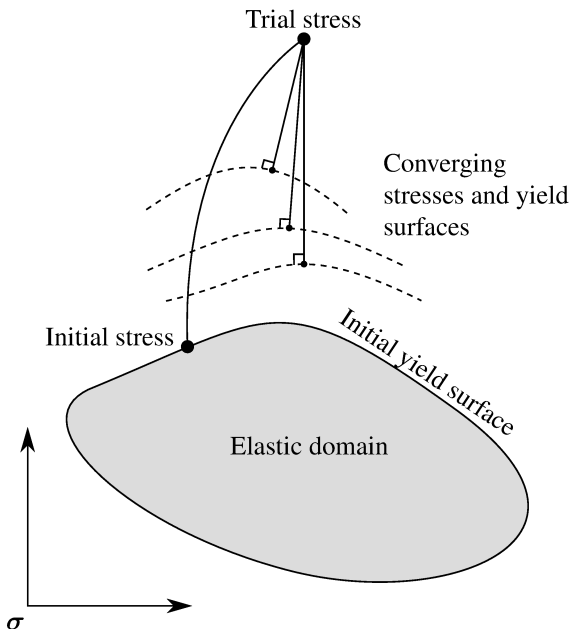

Figure 4. The closest point projection method in 2-D stress space (associated flow rule).

The aim of the CPP method is to satisfy the following conditions:

$$f(\boldsymbol{\sigma}, \boldsymbol{\mu}) \leq 0 \tag{38}$$

$$\boldsymbol{R} = 0 \tag{39}$$

$$\Delta\lambda \geq 0 \tag{40}$$

$$\Delta\lambda f(\boldsymbol{\sigma}, \boldsymbol{\mu}) = 0 \tag{41}$$

where $f(\boldsymbol{\sigma}, \boldsymbol{\mu}) = 0$ is the yield function which forms a surface in 3-D stress space, $\boldsymbol{\sigma}$ is the converged stress state, $\boldsymbol{\mu}$ represents one or more state variables which define the position of the yield surface, $\boldsymbol{R}$ is the residual of the plastic strains, and $\Delta\lambda$ is the variation in the plasticity multiplier which governs the size of the plastic strain steps.

As there are several yield surfaces present in the hardening soil model, and the evolution rules take different forms, a separate CPP algorithm is required for each yield surface and each possible combination of yield surfaces. The formulation of the CPP algorithms are documented in the following sections.

5.1. Single surface stress return

The role of the CPP algorithm for a single surface is to satisfy one yield criterion.

$$f(\boldsymbol{\sigma}, \boldsymbol{\sigma_{LC}}, \boldsymbol{\varepsilon^p}) = 0 \tag{42}$$

The plastic strain residual is given by

$$\boldsymbol{R} = -\boldsymbol{\Delta\varepsilon^p} + \Delta\lambda \frac{\partial g}{\partial \boldsymbol{\sigma}} = \boldsymbol{0} \tag{43}$$

Expanding Eq. 43 as a Taylor's series gives

$$\boldsymbol{R} + \boldsymbol{\delta R} = \boldsymbol{R} - \boldsymbol{\delta\varepsilon^p} + \delta\lambda \frac{\partial g}{\partial \boldsymbol{\sigma}} + \Delta\lambda \frac{\partial^2 g}{\partial \boldsymbol{\sigma}^2} \boldsymbol{\delta\sigma} = \boldsymbol{0} \tag{44}$$

Rearranging to obtain the plastic strain increment

$$\boldsymbol{\delta\varepsilon^p} = \boldsymbol{R} + \delta\lambda \frac{\partial g}{\partial \boldsymbol{\sigma}} + \Delta\lambda \frac{\partial^2 g}{\partial \boldsymbol{\sigma}^2} \boldsymbol{\delta\sigma} \tag{45}$$

Expanding Eq. 42 as a Taylor's series

$$f + \frac{\partial f}{\partial \boldsymbol{\sigma}}^T \boldsymbol{\delta\sigma} + \frac{\partial f}{\partial \boldsymbol{\varepsilon^p}}^T \boldsymbol{\delta\varepsilon^p} = \boldsymbol{0} \tag{46}$$

Substituting the plastic strain increment (Eq. 45) into Eq. 46

$$f + \frac{\partial f}{\partial \boldsymbol{\sigma}}^T \boldsymbol{\delta\sigma} + \frac{\partial f}{\partial \boldsymbol{\varepsilon^p}}^T \left(\boldsymbol{R} + \delta\lambda \frac{\partial g}{\partial \boldsymbol{\sigma}} + \Delta\lambda \frac{\partial^2 g}{\partial \boldsymbol{\sigma}^2} \boldsymbol{\delta\sigma} \right) = 0 \tag{47}$$

Grouping the $\boldsymbol{\delta\sigma}$ terms gives

$$f + \boldsymbol{F}^T \boldsymbol{\delta\sigma} + \frac{\partial s}{\partial \boldsymbol{\varepsilon^p}}^T \left(\boldsymbol{R} + \delta\lambda \frac{\partial g}{\partial \boldsymbol{\sigma}} \right) = 0 \tag{48}$$

where

$$\boldsymbol{F}^T = \frac{\partial f}{\partial \boldsymbol{\sigma}}^T + \Delta\lambda \frac{\partial f}{\partial \boldsymbol{\varepsilon^p}}^T \frac{\partial^2 g}{\partial \boldsymbol{\sigma}^2} \tag{49}$$

During the CPP iterations, the change in stress between iterations is

$$\boldsymbol{\delta\sigma} = -\boldsymbol{D_e}\boldsymbol{\delta\varepsilon^p} \tag{50}$$

Substituting the plastic strain increment (Eq. 45) into Eq. 50

$$\boldsymbol{\delta\sigma} = -\boldsymbol{D_e}\left(\boldsymbol{R} + \delta\lambda\frac{\partial g}{\partial\boldsymbol{\sigma}} + \Delta\lambda\frac{\partial^2 g}{\partial\boldsymbol{\sigma}^2}\boldsymbol{\delta\sigma}\right) \tag{51}$$

Rearranging Eq. 51 gives

$$\boldsymbol{\delta\sigma} = -\boldsymbol{A_e}\left(\boldsymbol{R} + \delta\lambda\frac{\partial g}{\partial\boldsymbol{\sigma}}\right) \tag{52}$$

where

$$\boldsymbol{A_e} = \left(\boldsymbol{I} + \Delta\lambda\boldsymbol{D_e}\frac{\partial^2 g}{\partial\boldsymbol{\sigma}^2}\right)^{-1}\boldsymbol{D_e} \tag{53}$$

and $\boldsymbol{I}$ is the identity matrix. Finally, the variation in the plasticity multiplier is calculated through substitution of Eq. 52 into Eq. 48 and rearranging for $\delta\lambda$.

$$\delta\lambda = \frac{f - \boldsymbol{F}^T\boldsymbol{A_e}\boldsymbol{R} + \frac{\partial f}{\partial\boldsymbol{\varepsilon^p}}^T\boldsymbol{R}}{\boldsymbol{F}^T\boldsymbol{A_e}\frac{\partial g}{\partial\boldsymbol{\sigma}} - \frac{\partial f}{\partial\boldsymbol{\varepsilon^p}}^T\frac{\partial g}{\partial\boldsymbol{\sigma}}} \tag{54}$$

5.2. Two surface stress return

When both surfaces are active, the stress state must return to the line which is the intersection of both surfaces. The formulation must also take into account the inter-dependency between the hardening rules of each surface.

The total plastic strain residual now incorporates hardening from both surfaces

$$\boldsymbol{R} = -\boldsymbol{\Delta\varepsilon^p} + \Delta\lambda_1\frac{\partial g_1}{\partial\boldsymbol{\sigma}} + \Delta\lambda_2\frac{\partial g_2}{\partial\boldsymbol{\sigma}} = \boldsymbol{0} \tag{55}$$

Expanding Eq. 55 as a Taylor's series and simplifying leads to a form of the plastic strain increment which involves both surfaces.

$$\begin{aligned}\boldsymbol{\delta\varepsilon^p} = \boldsymbol{R} &+ \delta\lambda_1\frac{\partial g_1}{\partial\boldsymbol{\sigma}} + \delta\lambda_2\frac{\partial g_2}{\partial\boldsymbol{\sigma}} \\ &+ \left(\Delta\lambda_1\frac{\partial^2 g_1}{\partial\boldsymbol{\sigma}^2} + \Delta\lambda_2\frac{\partial^2 g_2}{\partial\boldsymbol{\sigma}^2}\right)\boldsymbol{\delta\sigma}\end{aligned} \tag{56}$$

The expansion of the yield surfaces remain identical to Eq. 46, however the new definition of the plastic strain increment Eq. 56 must be substituted into Eq. 46. Grouping the $\boldsymbol{\delta\sigma}$ after this substitution leads to

$$f_1 + \boldsymbol{F_1}^T\boldsymbol{\delta\sigma} + \frac{\partial f_1}{\partial\boldsymbol{\varepsilon^p}}^T\left(\boldsymbol{R} + \delta\lambda_1\frac{\partial g_1}{\partial\boldsymbol{\sigma}} + \delta\lambda_2\frac{\partial g_2}{\partial\boldsymbol{\sigma}}\right) = 0 \tag{57}$$

where

$$\boldsymbol{F_1}^T = \frac{\partial f_1}{\partial\boldsymbol{\sigma}}^T + \frac{\partial f_1}{\partial\boldsymbol{\varepsilon^p}}^T\left(\Delta\lambda_1\frac{\partial^2 g_1}{\partial\boldsymbol{\sigma}^2} + \Delta\lambda_2\frac{\partial^2 g_2}{\partial\boldsymbol{\sigma}^2}\right) \tag{58}$$

and similarly for the second surface:

$$\boldsymbol{F_2}^T = \frac{\partial f_2}{\partial\boldsymbol{\sigma}}^T + \frac{\partial f_2}{\partial\boldsymbol{\varepsilon^p}}^T\left(\Delta\lambda_1\frac{\partial^2 g_1}{\partial\boldsymbol{\sigma}^2} + \Delta\lambda_2\frac{\partial^2 g_2}{\partial\boldsymbol{\sigma}^2}\right) \tag{59}$$

The two surface form of the plastic strain increment (Eq. 56) is now substituted into the incremental stress relationship (Eq. 50).

$$\begin{aligned}&\boldsymbol{\delta\sigma} = \\ &-\boldsymbol{D_e}\left[\boldsymbol{R} + \delta\lambda_1\frac{\partial g_1}{\partial\boldsymbol{\sigma}} + \delta\lambda_2\frac{\partial g_2}{\partial\boldsymbol{\sigma}} + \left(\Delta\lambda_1\frac{\partial^2 g_1}{\partial\boldsymbol{\sigma}^2} + \Delta\lambda_2\frac{\partial^2 g_2}{\partial\boldsymbol{\sigma}^2}\right)\boldsymbol{\delta\sigma}\right]\end{aligned} \tag{60}$$

The stress increment from Eq. 60 simplifies to

$$\boldsymbol{\delta\sigma} = -\boldsymbol{A_e}\left(\boldsymbol{R} + \delta\lambda_1\frac{\partial g_1}{\partial\boldsymbol{\sigma}} + \delta\lambda_2\frac{\partial g_2}{\partial\boldsymbol{\sigma}}\right) \tag{61}$$

where

$$\boldsymbol{A_e} = \left(\boldsymbol{I} + \Delta\lambda_1\boldsymbol{D_e}\frac{\partial^2 g_1}{\partial\boldsymbol{\sigma}^2} + \Delta\lambda_2\boldsymbol{D_e}\frac{\partial^2 g_2}{\partial\boldsymbol{\sigma}^2}\right)^{-1}\boldsymbol{D_e} \tag{62}$$

Substituting Eq. 61 into Eq. 57 and its second surface counterpart, then rearranging into matrix form gives an expression for the plasticity multipliers to be solved.

$$\boldsymbol{\Omega_f} = \boldsymbol{\Omega} \begin{bmatrix} \delta\lambda_1 \\ \delta\lambda_2 \end{bmatrix} \tag{63}$$

where

$$\boldsymbol{\Omega_f} = \begin{bmatrix} f_1 - \boldsymbol{F_1}^T \boldsymbol{A_e} \boldsymbol{R} + \frac{\partial f_1}{\partial \boldsymbol{\varepsilon^p}} \boldsymbol{R} \\ f_2 - \boldsymbol{F_2}^T \boldsymbol{A_e} \boldsymbol{R} + \frac{\partial f_2}{\partial \boldsymbol{\varepsilon^p}} \boldsymbol{R} \end{bmatrix} \tag{64}$$

$$\boldsymbol{\Omega} = \begin{bmatrix} \boldsymbol{F_1}^T \boldsymbol{A_e} \frac{\partial g_1}{\partial \boldsymbol{\sigma}} - \frac{\partial f_1}{\partial \boldsymbol{\varepsilon^p}}^T \frac{\partial g_1}{\partial \boldsymbol{\sigma}} & \boldsymbol{F_1}^T \boldsymbol{A_e} \frac{\partial g_2}{\partial \boldsymbol{\sigma}} - \frac{\partial f_1}{\partial \boldsymbol{\varepsilon^p}}^T \frac{\partial g_2}{\partial \boldsymbol{\sigma}} \\ \boldsymbol{F_2}^T \boldsymbol{A_e} \frac{\partial g_1}{\partial \boldsymbol{\sigma}} - \frac{\partial f_2}{\partial \boldsymbol{\varepsilon^p}}^T \frac{\partial g_1}{\partial \boldsymbol{\sigma}} & \boldsymbol{F_2}^T \boldsymbol{A_e} \frac{\partial g_2}{\partial \boldsymbol{\sigma}} - \frac{\partial f_2}{\partial \boldsymbol{\varepsilon^p}}^T \frac{\partial g_2}{\partial \boldsymbol{\sigma}} \end{bmatrix} \tag{65}$$

Eq. 63 is then solved for the unknown plasticity multipliers $\delta\lambda_1$ and $\delta\lambda_2$.

5.3. Additional CPP considerations

The CPP formulations in this section are described in terms of a generic case where the hardening rule is related directly to the plastic strain vector $\boldsymbol{\varepsilon^p}$. Hence, the algorithms can be used directly for the shear and tension surfaces. The tension surface does not harden, therefore the hardening term $\frac{\partial f_t}{\partial \boldsymbol{\varepsilon^p}}$ is equal to zero.

The cap surface uses an incremental form for the hardening rule, therefore a hardening residual must be included in the formulation.

$$R_h = -\Delta p_p + \Delta\lambda \frac{\partial p_p}{\partial \varepsilon_v^p} \frac{\partial \varepsilon_v^p}{\partial \boldsymbol{\varepsilon^p}}^T \frac{\partial g_c}{\partial \boldsymbol{\sigma}} = 0 \tag{66}$$

The Taylor's series expansion of the yield function also includes the hardening parameter p_p directly. The plasticity multiplier for the cap surface is calculated using this hardening residual.

$$\delta\lambda_c = \frac{f_c - \boldsymbol{F_c}^T \boldsymbol{A_e} \boldsymbol{R} + \frac{\partial f_c}{\partial p_p} R_h}{\boldsymbol{F_c^T} \boldsymbol{A_e} \frac{\partial g_c}{\partial \boldsymbol{\sigma}} - \frac{\partial f_c}{\partial p_p} \frac{\partial p_p}{\partial \varepsilon_v^p} \frac{\partial \varepsilon_v^p}{\partial \boldsymbol{\varepsilon^p}}^T \frac{\partial g_c}{\partial \boldsymbol{\sigma}}} \tag{67}$$

5.4. Return mapping procedure
5.5. Return mapping procedure

As the HS-LC model uses multiple hardening yield surfaces and uses a non-associated flow rule, a simple zoning method is not sufficient to detect which surfaces are active for a given trial stress. Instead, a more complex approach is adopted which returns the stress to each surface in turn, then checks other surfaces for yielding. Figure 5 illustrates the order in which yield criteria are checked and returned to (following from Benz (2007)). The primary and most dominant surface in the HS and HS-LC models is the shear surface, hence the trial stress state $\boldsymbol{\sigma_{tr}}$ and plastic strains $\boldsymbol{\varepsilon^p}$ are checked against the shear surface $f_s = 0$ (Eq. 28). If this yield criterion is exceeded, then the single surface CPP algorithm is used to return the stress state to the shear surface.

After the return to the shear surface, it may be possible that one of the other yield criteria are exceeded. Following a shear surface return, the cap yield function $f_c = 0$ (Eq. 20) is checked with the returned stress and state variables. If the cap criterion is exceeded, two surface hardening is not automatically assumed, and the stress is returned to the cap surface using the single surface CPP algorithm from the trial stress $\boldsymbol{\sigma_{tr}}$ and starting state variables. If the shear yield criterion is still exceeded after the cap return, then the two surface CPP algorithm is used. Unless the soil analysed is heavily over-consolidated, this combination of surfaces is the most commonly used in primary loading.

A similar procedure is adopted for the tensile yield surface $f_t = 0$ (Eq. 36). After the first shear surface return, the tensile criterion is checked. If exceeded, then the single surface CPP algorithm is used to return the stress and state variables to the tension yield surface. If the shear criterion is still exceeded, then the two surface CPP algorithm is used.

In the case that the shear surface is not initially yielding, the cap surface yield criterion is checked and returned to if necessary. This cap return may place the updated stress in a region which exceeds the shear yield criterion. If the shear yield criterion is exceeded, then the two surface CPP algorithm is used to return the stress and state variables to the shear and cap surfaces. The tension surface does not need to be checked here because the tension and cap surfaces cannot both be active.

Finally, if no yielding was detected before this stage, then the tensile yield criterion $f_t = 0$ (Eq. 36) is checked and returned to if this criterion is exceeded. The shear criterion does not need to be checked again because shear yielding would have been detected at the first stage.

5.6. Example CPP algorithm

Algorithm 1 describes the most complex of the CPP algorithms, namely the return to the shear and cap surfaces. It is the most complex because it includes reduction of the cap hardening residual R_h due to the decoupling of the two surfaces.

To convert this algorithm to return to the shear and tension surfaces, the subscript c is replaced with t. The tension surface

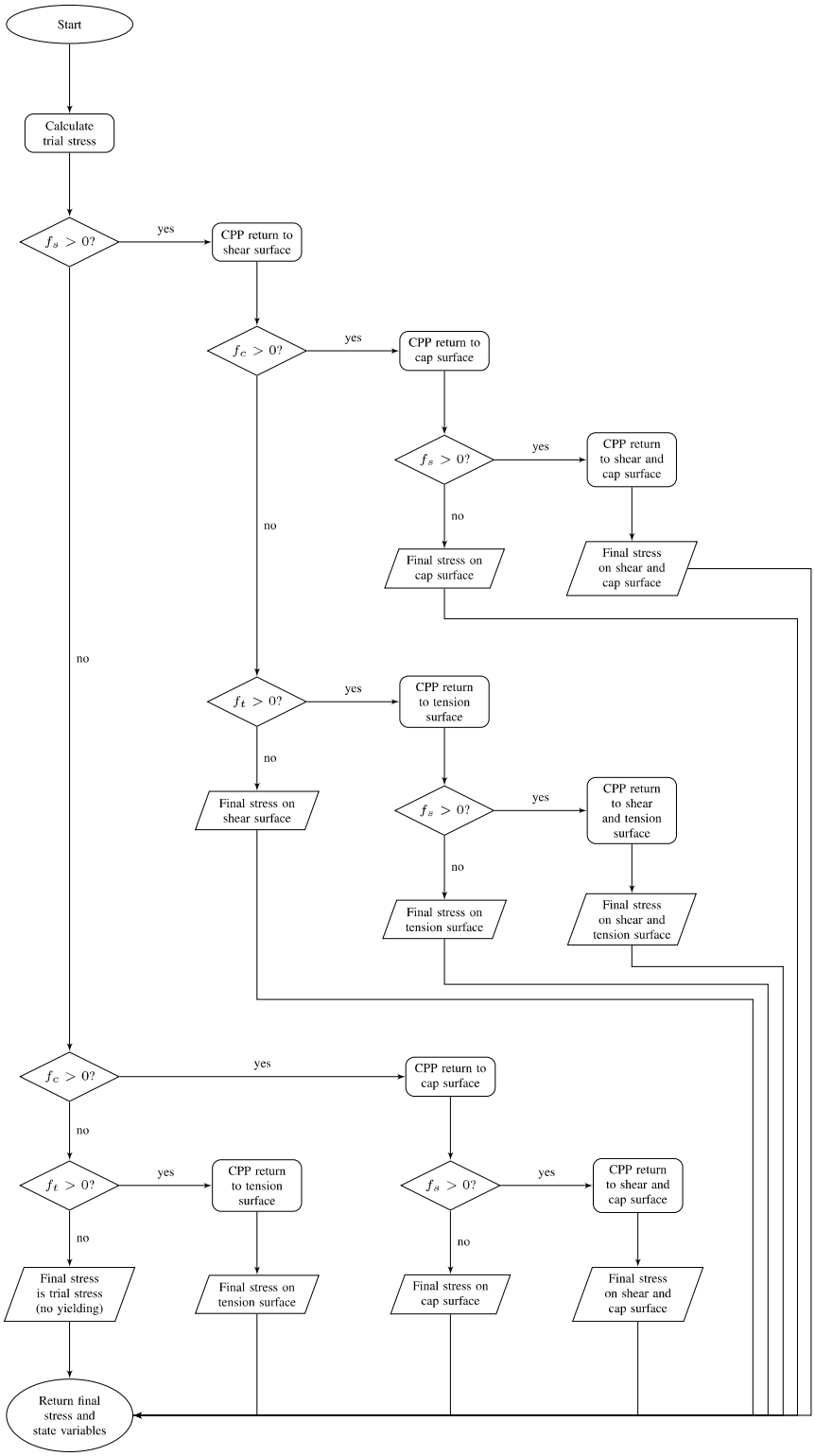

Figure 5. Return mapping algorithm used in the HS-LC model: Each yield function and return mapping algorithm are referenced as follows; f_s - Eq. 28; f_c - Eq. 20; f_t - Eq. 36; CPP shear - Eqs. 42 to 54 with subscript s; CPP cap - Eqs. 42 to 54, subscript c, and hardening residual (Eq. 66); CPP tension - Eqs. 42 to 54, subscript t; CPP shear & cap - Eqs. 55 to 63, subscripts s and c, and cap hardening residual (Eq. 66); CPP shear & tension - Eqs. 55 to 63, subscripts s and t.

uses an associated flow rule ($g_t \equiv f_t$). Additionally, the tension surface is non-hardening, therefore $\frac{\partial f_t}{\partial \boldsymbol{\varepsilon^p}} = \mathbf{0}$ in each of the relevant expressions.

The procedure for the single surface CPP algorithms is similar to those of the double surface procedure. The stress increment, plastic strain increment, and pseudo-consistent constitutive matrix contain derivatives for one surface only. The calculation of the plasticity multiplier $\delta\lambda$ is performed using Eq. 54.

Algorithm 1 Closest Point Projection algorithm for HS-LC shear and cap surfaces.

Initialisation
$\Delta\lambda_s = 0; \delta\lambda_s = 0$
$\Delta\lambda_c = 0; \delta\lambda_c = 0$
$\Delta\varepsilon^p = 0; \boldsymbol{\varepsilon^p} = \boldsymbol{\varepsilon^p}, n-1$
$p_p = p_p^{n-1}$
$i = 1$
Trial stress
$\boldsymbol{\sigma} = \boldsymbol{\sigma_0} + \boldsymbol{D_e \Delta\varepsilon}$
Update yield functions
$f_s = f_s(\boldsymbol{\sigma}, \boldsymbol{\varepsilon^p})$
$f_c = f_c(\boldsymbol{\sigma}, p_p)$
$f_{s,tol} = |f_s| \cdot f_{tol}$
$f_{c,tol} = |f_c| \cdot f_{tol}$
while ($|f_s| > f_{s,tol}$ or $|f_c| > f_{c,tol}$ or $\|\boldsymbol{R}\| > R_{tol}$ or $|R_h| > R_{tol}$) and $i < i_{max}$ **do**
Calculate derivatives
$\frac{\partial f_s}{\partial \boldsymbol{\sigma}}; \frac{\partial g_s}{\partial \boldsymbol{\sigma}}; \frac{\partial^2 g_s}{\partial \boldsymbol{\sigma}^2}; \frac{\partial f_s}{\partial \boldsymbol{\varepsilon^p}}$
$\frac{\partial f_c}{\partial \boldsymbol{\sigma}}; \frac{\partial g_c}{\partial \boldsymbol{\sigma}}; \frac{\partial^2 g_c}{\partial \boldsymbol{\sigma}^2}; \frac{\partial f_c}{\partial p_p}; \frac{\partial p_p}{\partial \varepsilon_v^p}; \frac{\partial \varepsilon_v^p}{\partial \boldsymbol{\varepsilon^p}}$
Calculate pseudo-consistent constitutive matrix
$\boldsymbol{A_e} = \left(\boldsymbol{I} + \Delta\lambda_s \boldsymbol{D_e} \frac{\partial^2 g_s}{\partial \boldsymbol{\sigma}^2} + \Delta\lambda_c \boldsymbol{D_e} \frac{\partial^2 g_c}{\partial \boldsymbol{\sigma}^2}\right)^{-1} \boldsymbol{D_e}$
Calculate residual plastic strain and hardening parameter residual
$\boldsymbol{R} = -\boldsymbol{\Delta\varepsilon^p} + \Delta\lambda_s \frac{\partial g_s}{\partial \boldsymbol{\sigma}} + \Delta\lambda_c \frac{\partial g_c}{\partial \boldsymbol{\sigma}}$
$R_h = -\Delta p_p + \Delta\lambda_c \frac{\partial p_p}{\partial \varepsilon_v^p} \frac{\partial \varepsilon_v^p}{\partial \boldsymbol{\varepsilon^p}}^T \frac{\partial g_c}{\partial \boldsymbol{\sigma}}$
Stress increment
$\boldsymbol{\delta\sigma} = -\boldsymbol{A_e}\left(\boldsymbol{R} + \delta\lambda_s \frac{\partial g_s}{\partial \boldsymbol{\sigma}} + \delta\lambda_c \frac{\partial g_c}{\partial \boldsymbol{\sigma}}\right)$
Plasticity multipliers
$$\boldsymbol{\Omega} = \begin{bmatrix} \boldsymbol{F_s}^T \boldsymbol{A_e} \frac{\partial g_s}{\partial \boldsymbol{\sigma}} - \frac{\partial f_s}{\partial \boldsymbol{\varepsilon^p}}^T \frac{\partial g_s}{\partial \boldsymbol{\sigma}} & \boldsymbol{F_s}^T \boldsymbol{A_e} \frac{\partial g_c}{\partial \boldsymbol{\sigma}} - \frac{\partial f_s}{\partial \boldsymbol{\varepsilon^p}}^T \frac{\partial g_c}{\partial \boldsymbol{\sigma}} \\ \boldsymbol{F_c}^T \boldsymbol{A_e} \frac{\partial g_s}{\partial \boldsymbol{\sigma}} & \boldsymbol{F_c}^T \boldsymbol{A_e} \frac{\partial g_c}{\partial \boldsymbol{\sigma}} - \frac{\partial f_c}{\partial p_p} \frac{\partial p_p}{\partial \varepsilon_v^p} \frac{\partial \varepsilon_v^p}{\partial \boldsymbol{\varepsilon^p}}^T \frac{\partial g_c}{\partial \sigma} \end{bmatrix}$$
$$\boldsymbol{\Omega_f} = \begin{bmatrix} f_s - \boldsymbol{F_s}^T \boldsymbol{A_e} \boldsymbol{R} + \frac{\partial f_s}{\partial \boldsymbol{\varepsilon^p}} \boldsymbol{R} \\ f_c - \boldsymbol{F_c}^T \boldsymbol{A_e} \boldsymbol{R} + \frac{\partial f_c}{\partial p_p} R_h \end{bmatrix}$$
$$\begin{bmatrix} \delta\lambda_s \\ \delta\lambda_c \end{bmatrix} = \boldsymbol{\Omega}^{-1} \boldsymbol{\Omega_f}$$
$\Delta\lambda_s = \Delta\lambda_s + \delta\lambda_s$
$\Delta\lambda_c = \Delta\lambda_c + \delta\lambda_c$
Update plastic strains
$\boldsymbol{\delta\varepsilon^p} = \boldsymbol{R} + \delta\lambda_s \frac{\partial g_s}{\partial \boldsymbol{\sigma}} + \delta\lambda_c \frac{\partial g_c}{\partial \boldsymbol{\sigma}} + \left(\Delta\lambda_s \frac{\partial^2 g_s}{\partial \boldsymbol{\sigma}^2} + \Delta\lambda_c \frac{\partial^2 g_c}{\partial \boldsymbol{\sigma}^2}\right) \boldsymbol{\delta\sigma}$
$\boldsymbol{\Delta\varepsilon^p} = \boldsymbol{\Delta\varepsilon^p} + \boldsymbol{\delta\varepsilon^p}$
$\boldsymbol{\varepsilon^p} = \boldsymbol{\varepsilon^p} + \boldsymbol{\delta\varepsilon^p}$
Update stress
$\boldsymbol{\sigma} = \boldsymbol{\sigma} + \boldsymbol{\delta\sigma}$
Re-calculate yield functions
$f_s = f_s(\boldsymbol{\sigma}, \boldsymbol{\varepsilon^p})$
$f_c = f_c(\boldsymbol{\sigma}, p_p)$
$i = i + 1$
end while
Check convergence
if $|f_s| > f_{s,tol}$ or $|f_c| > f_{c,tol}$ or $\|\boldsymbol{R}\| > R_{tol}$ or $|R_h| > R_{tol}$ **then**
output an error message and stop the program
end if
return $\boldsymbol{\sigma}, \boldsymbol{\varepsilon^p}, p_p, \Delta\lambda_s, \Delta\lambda_c$

6. Consistent tangent matrix

The consistent tangent matrix (CTM) relates infinitesimal stresses and strains. It is used to calculate the stress gradients on one or more active yield surfaces and preserves the quadratic rate of convergence in the global Newton-Raphson iterative scheme.

Much of the theory for defining the consistent tangent matrix has been discussed already, however it is worth noting that in the formulation of the CTM, the stress state is assumed to already be on one or more yield surfaces and the residuals relating to the active surface(s) are zero. The plastic multiplier(s) $\Delta\lambda$ from the previous iteration are also required. The consistent tangent is defined as:

$$\boldsymbol{D_{ep}} = \frac{\mathrm{d}\boldsymbol{\sigma}}{\mathrm{d}\boldsymbol{\varepsilon}} \tag{68}$$

If the stress state lies on a single yield surface, then the consistent tangent is given as

$$\boldsymbol{D_{ep}} = \boldsymbol{A_e} - \frac{\boldsymbol{A_e} \frac{\partial g}{\partial \boldsymbol{\sigma}} \boldsymbol{F}^T \boldsymbol{A_e}}{\boldsymbol{F}^T \boldsymbol{A_e} \frac{\partial g}{\partial \boldsymbol{\sigma}} - \frac{\partial f}{\partial \boldsymbol{\varepsilon^p}}^T \frac{\partial g}{\partial \boldsymbol{\sigma}}} \tag{69}$$

When two surfaces are active, a more complex approach is used which takes into account the gradients and hardening rules from both surfaces.

$$\begin{aligned} \boldsymbol{D_{ep}} = \boldsymbol{A_e} &- \left(\Omega^{-1}\right)_{1,1} \boldsymbol{A_e} \frac{\partial g_1}{\partial \boldsymbol{\sigma}} \boldsymbol{F_1}^T \boldsymbol{A_e} \\ &- \left(\Omega^{-1}\right)_{1,2} \boldsymbol{A_e} \frac{\partial g_1}{\partial \boldsymbol{\sigma}} \boldsymbol{F_2}^T \boldsymbol{A_e} \\ &- \left(\Omega^{-1}\right)_{2,1} \boldsymbol{A_e} \frac{\partial g_2}{\partial \boldsymbol{\sigma}} \boldsymbol{F_1}^T \boldsymbol{A_e} \\ &- \left(\Omega^{-1}\right)_{2,2} \boldsymbol{A_e} \frac{\partial g_2}{\partial \boldsymbol{\sigma}} \boldsymbol{F_2}^T \boldsymbol{A_e} \end{aligned} \tag{70}$$

7. Additional computational considerations

During preliminary testing of the HS-LC model, it was found that some step size dependency occurred when modelling certain simulations. In the initial implementation of the HS-LC model, the Young modulus used in the calculation of the elastic and tangent stiffness matrices was based on the converged stress from the previous increment. Use of the last converged modulus significantly improves the stability of the model, as the non-linearity within a given increment is reduced. For large step sizes, this causes the results to drift from the true solution.

A simple method to reduce the step size dependency could be to directly update Young's modulus in every iteration; however, this was found to increase the non-linearity in the model and analyses would converge poorly. An alternative approach is proposed: this involves updating the Young's modulus for a controlled number

of iterations at the start of each increment. Within each iteration, Young's modulus is frozen; this retains stability in the local iterative procedure.

It is acknowledged that the stiffness calculated as a result of the update of Young's modulus may be approximate, as the solution would not be converged. Therefore, some dependency on the last converged solution can be used by introducing a weighting factor, such that Young's moduli are a function of the last converged stress $\boldsymbol{\sigma_{LC}}$ and the stress from the previous iteration $\boldsymbol{\sigma_{LI}}$; i.e.

$$E_{ur}\left((1-r)\,\boldsymbol{\sigma_{LC}} + r\boldsymbol{\sigma_{LI}}\right) \tag{71}$$

where r is the weighting factor which controls the dependency on the last converged stress. A value of $r = 0$ forces the model to use only the last converged stress $\boldsymbol{\sigma_{LC}}$, and a value of $r = 1$ forces the model to use only the stress from the last increment $\boldsymbol{\sigma_{LI}}$. This update is performed until the absolute relative change in Young's moduli ΔE between iterations reduces to below a given tolerance.

$$\Delta E = \frac{\left|E_{ur} - (E_{ur})_{LI}\right|}{E_{ur}} \tag{72}$$

As each of Young's moduli E_{ur} and E_i are linearly proportional to one-another, any one of them may be used to determine the change in the moduli; in the proposed model, the unloaded modulus E_{ur} is selected.

Within a given increment, the tangent matrix can be considered to be consistent, in that it describes the infinitesimal relationship between stress and strain as defined in the rest of the model. However, from a more global perspective, it is more correct to describe this as a pseudo-consistent tangent, this is because some of the variables are effectively frozen between iterations.

8. Results and discussions

The HS-LC model has been implemented in finite element analysis software LUSAS for the purpose of solving boundary value problems. Case studies with experimental data and predictions with other models were chosen to compare with the HS-LC model. The first problem is a one-dimensional oedometer test on a dry sand; experimental data, and predictions from the original HS model were extracted from the paper by Schanz et al. (1999). The second problem is a triaxial compression test on the same sand, again, experimental data and predictions from the original HS model are also available Schanz et al. (1999). These two tests are chosen to demonstrate the capabilities of the HS-LC model in reproducing common soil laboratory tests. The parameters used in the HS-LC model for each analysis are shown in Table 1. The calibration parameters which these are adjusted to are: $E_{50}^{ref} = 23,890$ kPa, $E_{oed}^{ref} = 16,500$ kPa, $K_0 = 0.44$.

Results from previous experiments and predictions with the HS model Schanz et al. (1999) were extracted through interpretation of graphs. Hence, it is expected that there may some minor differences with these results. For the purposes of this study where two models are being compared at a broad level, these differences should be sufficiently insignificant.

Finally, a third set of analyses are performed on a hypothetical embankment using both a plane-strain, and a 3D analysis. The factor of safety of the slope is determined using φ-c reduction. This result is compared against the factor of safety determined through analytical and graphical methods.

Table 1. Material parameters used in the HS-LC model simulations.

	Loose Hostun sand	Embankment soil
ρ (kg/m^3)		1.4
ν	0.2	0.35
φ ($^\circ$)	34	30
ψ ($^\circ$)	1.5	0.0
c (kPa)	0.0	50.0
m	0.65	0.50
R_f	0.95	0.90
E_{ur}^{ref} (kPa)	60,000	60,000
E_i^{ref} (kPa)	68,913	25,000
K_s/K_c	1.75	2.00
α	0.959	1.000
σ_t (kPa)	0	283

8.1. Oedometer test

This test considers the stress-strain response of confined uniaxial compression of loose Hostun sand (Table 1). The problem was modelled using a 4 by 4 grid of quadratic, quadrilateral axisymmetric elements. The oedometer sample modelled was of height and radius 3.5 cm; the base of the soil was fully fixed and the outside vertical boundary was fixed in the horizontal direction. A prescribed displacement was applied to the top of the soil in the vertical direction, 4 unloading-reloading cycles were used and the analysis was performed using a total of 243 increments with a loading and unloading rate of 0.2 mm per increment. The full load curve for this test can be found in Figure 6.

Experimental and predicted results are presented by (Schanz et al., 1999). Whilst a number of material parameters for the loose Hostun sand were described, a some material parameters were not available; including the oedometer modulus E_{oed}^{ref}. For this study, the oedometer modulus was determined from the

published experimental results by calculating the gradient of the oedometer curve at the reference stress $\sigma^{ref} = -100$ kPa. The remaining stiffness parameters E_{50}^{ref} and E_{ur}^{ref} were determined by measuring the secant stiffness and unload-reload stiffness from the published triaxial data. The auxiliary parameters α and K_s/K_c were calibrated to E_{oed} and to an assumed value of the lateral earth pressure coefficient $K_0 = 1 - \sin\varphi$. A small dilatancy angle was also used to reflect the volumetric strain increase observed in the experimental triaxial data. The full list of material parameters can be found in Table 1. The results of the oedometer simulation are plotted in Figure 7.

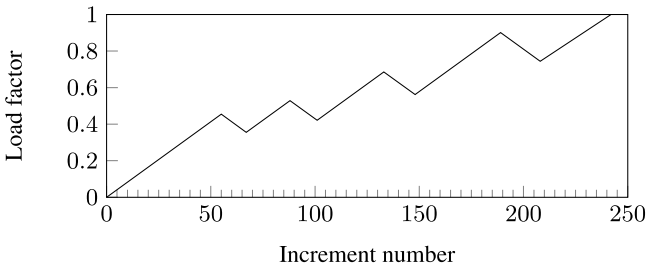

Figure 6. Load factor progression for the oedometer test.

The prediction of the primary loading curve closely matches the experimental data below 0.02 axial strain. The published experimental reloading cycle is incomplete after this stage.

The unloading cycles initially under-predict the stiffness, however the stiffness is predicted well in the third and fourth cycles. The experimental data shows different paths between unloading and reloading; this is something not captured in the HS and HS-LC models because elastic stiffness is assumed when below the yield surface.

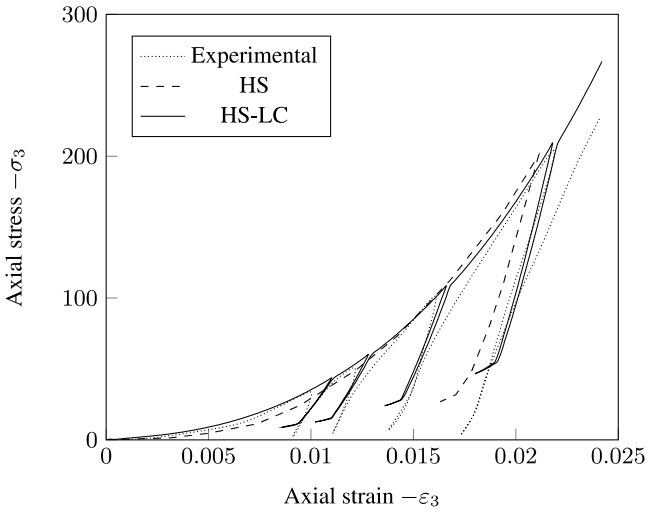

Figure 7. Oedometer test results and predictions for the HS model (Schanz et al., 1999), and the HS-LC model.

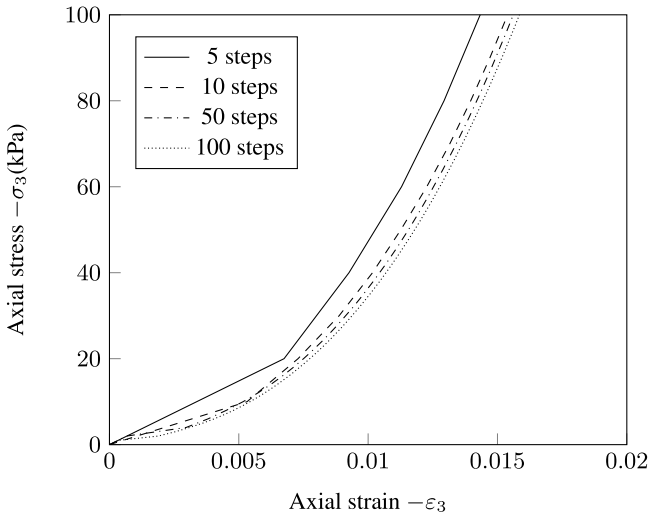

Figure 8. Oedometer test step size study using stiffness update procedure with $r = 0.33$; the stiffness was updated until $\Delta E \leq 0.05$.

Another interesting feature of the HS and HS-LC predictions is the change in gradient towards the end of each unloading stage. This was found to be caused by the minor principal stress swapping orientation. This stress component is used to calculate Young's modulus (Eq. 11). It may be possible to remove this phenomenon in the HS and HS-LC models by using a stiffness dependency based on the mean stress.

As might be expected for a simple test, relatively few iterations are required to achieve convergence in each step, with each increment requiring only 2 iterations to converge to the given tolerances. The global tolerances used for this test, and all other tests in this study are as follows: the residual force norm tolerance is 0.001%, and the incremental displacement norm tolerance is 0.001%.

A second series of oedometer simulations were carried out to investigate the impact of step size in the HS-LC model. These analyses were stress-controlled and the soil is taken to a vertical load of 100 kPa using different step sizes.

Figure 8 shows that the model is step size convergent when the load is split into at least 10 steps. Minor differences in the response relate to the stiffness update procedure but the differences are considered negligible for the 10, 50, and 100 step tests. However, this procedure comes at a cost of increasing the total number of iterations per increment; this has been documented previously (Bower, 2017). As the stiffness of the problem changes, the global rate of convergence is lowered slightly. This effect is most

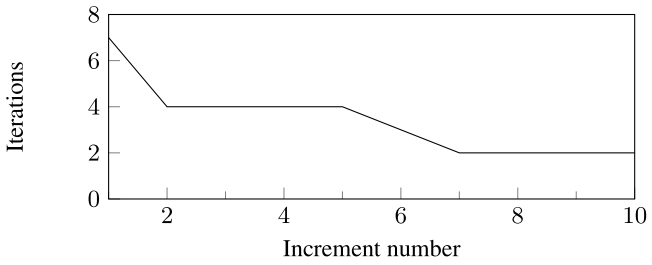

Figure 9. Number of iterations until convergence for the 10 step oedometer simulation.

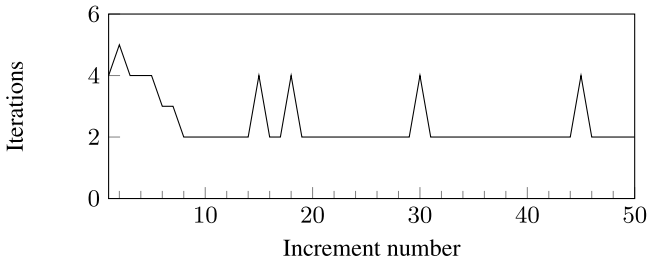

Figure 10. Number of iterations until convergence for the 50 step oedometer simulation.

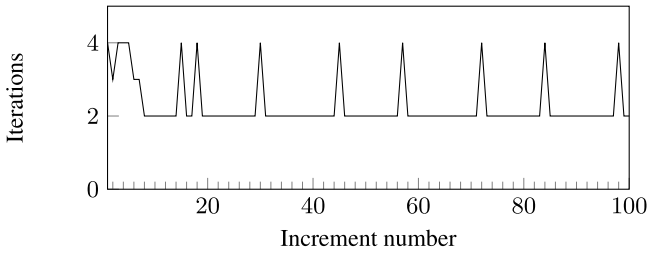

Figure 11. Number of iterations until convergence for the 100 step oedometer simulation.

prominent at the start of the test and can be seen in Figures 9 to 11, where the first few increments converge in 4 or more iterations. The remainder of each test converged in 4 increments or fewer, with most converging in 2 iterations. For the 5 step test, each of the increments took 4 iterations to converge.

Bower (2017) showed that use of the stiffness update procedure was necessary to preserve accuracy in the load paths of problems in which stress-dependent stiffness is an important factor. A similar comparison was performed with oedometer tests both with and without the stiffness update procedure. Without the update procedure, the oedometer tests using 250 and 500 steps produced similar load paths, however, the 50 and 100 step tests deviated from these other tests to a much greater degree than that shown in Figure 8.

8.2. Triaxial compression test

A drained, normally-consolidated triaxial test was simulated using the same material properties as the oedometer test (Table 1). Experimental data and predictions from the original HS model were also found for this test (Schanz et al., 1999). The experimental and predicted shear response is plotted in Figure 12, and the volumetric responses are plotted in Figure 13.

The problem was analysed using a single axisymmetric element, the radius of the triaxial cell was taken to be 3 cm and the height was taken to be 10 cm. The base of the cell was fixed in the vertical direction and the axis of symmetry was fixed in the horizontal direction. The soil was prescribed an initial isotropic compressive stress of 300 kPa to simulate the effective confining stress. A vertical displacement was applied to the top of the soil at a rate of 0.03 cm per increment for 50 increments.

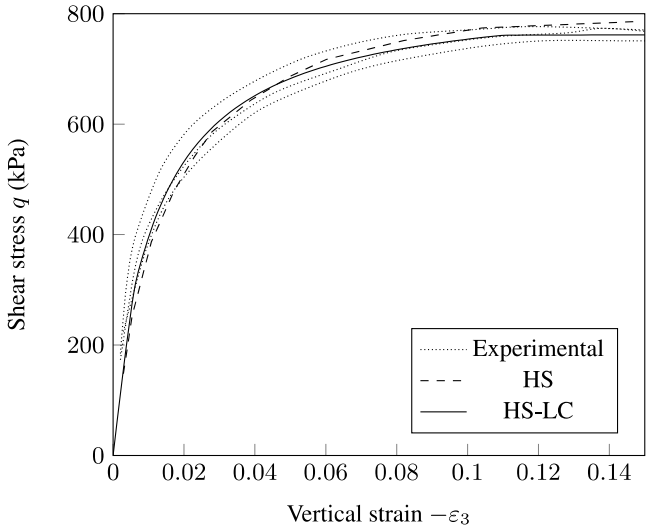

Figure 12. Triaxial test shear plots for simulation and 3 repeated experimental plots at 300 kPa confining stress.

The prediction of the shear stress response, as shown in Figure 12, follows a similar path to the original HS model, which slightly under-predicts the initial stiffness and the HS-LC provides a closer match. The shear stress failure limit for the HS-LC model can be seen to come into effect after $\varepsilon_3 = -0.11$, and the maximum shear stress matches the original HS model and the experimental curves.

The predictions of the volumetric strain (Figure 13) vary between the HS and HS-LC models. The HS-LC model predicts an increased compaction at the start of the simulation compared to the experimental results and the HS model. Including the small dilatancy angle has caused the soil to dilate with increasing shear stress. The post-failure gradient matches the experimental results well. The modified Rowe dilatancy formula (Eq. 13) is used in this

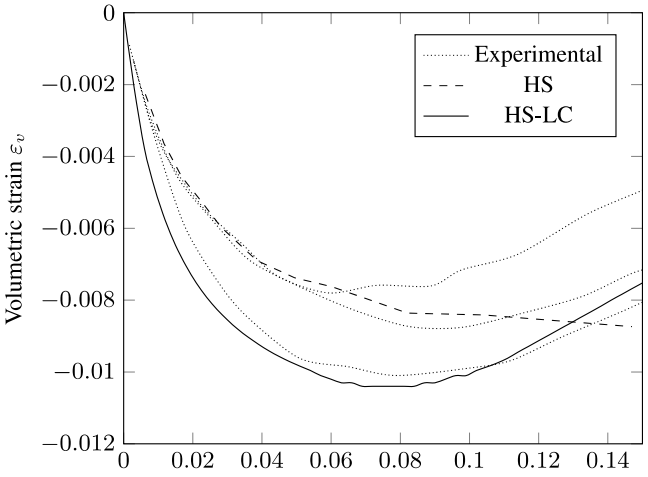

Figure 13. Triaxial test volumetric plots for simulation and 3 repeated experimental plots at 300 kPa confining stress.

simulation. The difference with the initial gradient between the two models is likely due to the dilatancy rules used in each model.

From the convergence plot for the triaxial test simulation (Figure 14), the first 2 increments converged in 3 iterations, this decreased to 2 iterations per increment until increment 20, where most increments converged in 1 iteration. On initial investigation with the original HS model, it was found that this test required an increasing number of iterations to converge as the test progressed, and a sharp increase in required iterations was observed as the shear stress approached the Mohr-Coulomb failure limit. By making the changes to the HS model proposed in this paper, this problem was overcome.

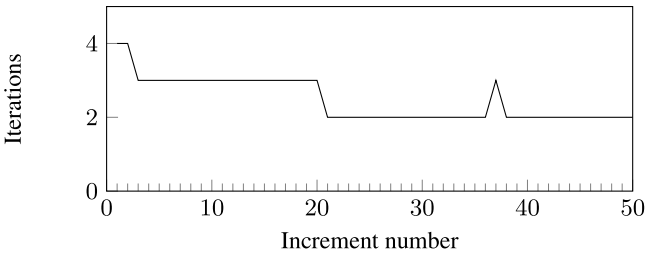

Figure 14. Number of iterations until convergence for the triaxial test.

8.3. Slope stability analysis with φ-c reduction

In this section, the factor of safety (FOS) of a slope due to its self weight is determined using the φ-c reduction technique, which is compared against an analytical and a graphical method.

The main principal of the φ-c strength reduction method is to reduce the values of the friction angle φ and cohesion c such that the failure criterion is reduced in overall size. The parameters are reduced by the following relationships according to the FOS F.

$$c^* = \frac{c}{F} \tag{73}$$

$$\varphi^* = \tan\left(\frac{\arctan\varphi}{F}\right) \tag{74}$$

where c^* and φ^* are the reduced set of failure parameters. In the HS-LC model, when the φ-c code is activated, the hardening shear surface is deactivated and replaced with the Matsuoka-Nakai failure criterion in its final position. This is performed by setting $r_q = R_f$ in Eq. 27. The stress dependent parameters E_i, E_{ur}, and $\sin\psi_m$ are also frozen. Except for the dilatancy angle ψ_m, which is set to the minimum of the frozen value of ψ_m and φ^*. The cap yield surface is also removed from the analysis during φ-c reduction, as it merely describes the evolution of plastic variables rather than soil failure.

In LUSAS, the FOS F is adjusted using an automatic procedure until the stiffness of any part of the soil reaches a sufficiently small value (i.e. global failure).

In the following example, the height of the slope is 10 m and steepness is 45°. The mesh is extended 20 m beyond the end of the slope, which is considered sufficient to minimise boundary effects. The 2D mesh (Figure 15) comprises of 2,933 nodes and 2,816 linear, quadrilateral plane-strain elements.

The full HS-LC model was utilised in the initiation of stresses due to self-weight up until the point where the strength reduction procedure commenced, when the shear surface becomes locked to match the position of the failure surface.

The embankment was initialised in 4 equal lifts of 2.5 m each. First, the flat domain of the soil was initialised under gravity loading ($g = 9.807$ m/s^2). Each lift was then activated and gravity was applied to each layer as it was activated using automatic load incrementation. The Young modulus update described in Section 7 was not used here as it was determined to not have any influence on the final calculated FOS.

An analytical analysis of the same slope was performed using the ordinary method of slices (OMS). This analysis was performed using the WISE Uranium project slope stability calculator World Information Service on Energy (2014) whereby the FOS at a series of centre points and radii were determined. The area around the minimum FOS was then scanned in more detail to further minimise the calculated FOS.

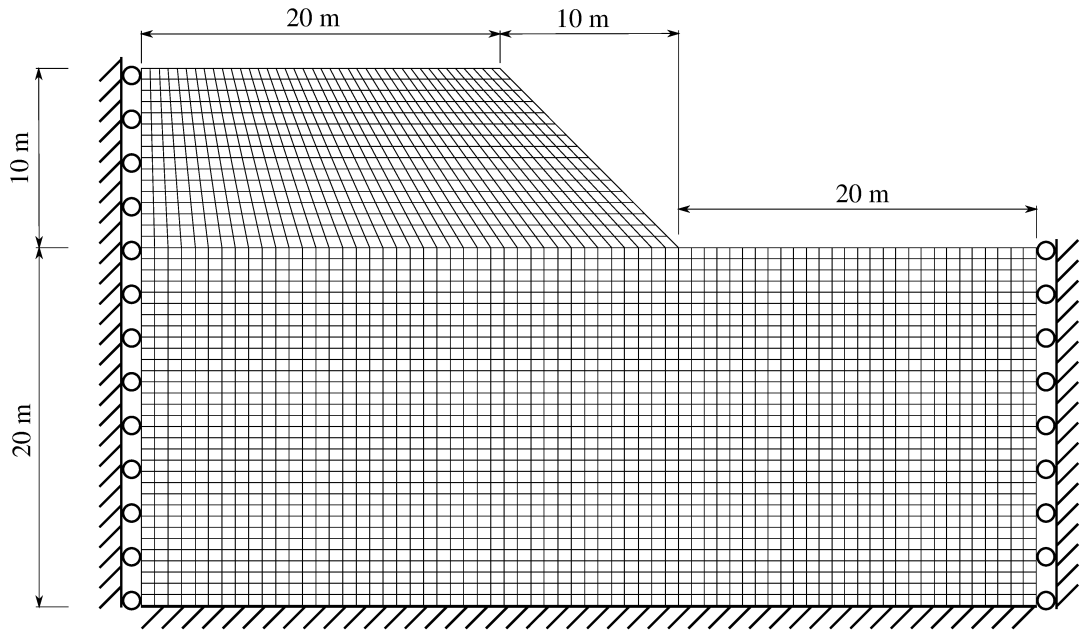

Figure 15. Mesh, geometry, and boundary conditions of the plane-strain slope stability problem.

A graphical method for determining the FOS for a uniform, drained slope was also used Steward et al. (2010). This is a non-iterative graphical method which produces two versions of the FOS; the first places emphasis on the cohesion c, and the second on the friction angle φ. The results from the analytical method, graphical method, and φ-c reduction method are shown in Table 2.

Table 2. Factor of safety for the slope calculated through different methods.

OMS	Graphical (c)	Graphical (φ)	φ-c reduction
3.284	3.403	3.174	3.054

The calculated values of the factor of safety from each of the methods tested in this paper are broadly similar. From a geotechnical perspective, these values are close enough to be considered equivalent for design purposes. The FOS calculated through the φ-c reduction method is slightly below those calculated through the other tested methods, making it a more conservative prediction.

From Figure 16, the failure mechanism of this slope is near circular, with the slip circle originating at the toe of the slope. From the ordinary method of slices, the slip circle with the lowest FOS was determined to have a centre 15.0 m directly above the toe of the slope with a radius of 15.0 m. The lower section of the HS-LC slip surface matches this well, however, the top section in the HS-LC analysis forms more of a wedge type failure. The OMS method was limited to circular slip surfaces, therefore a closer match to the HS-LC results may be attainable with different slip surface shapes.

The contour plots of the shear strain γ (Figure 17) show more precisely the location of shear failure in the soil. The highest shear strain can be found at a point about 5.0 m horizontal to a point just above the toe of the slope.

A second analysis of the slope was performed with modified boundary conditions. This particular case study is not included as a validation or benchmark but as a demonstration of the HS-LC model's 3D capabilities.

The 3D mesh (Figure 18) was formed from of 12,208 nodes and 10,560 linear, 8-noded hexahedral elements. The boundary conditions were modified from plane-strain conditions such that one side of the 'slice' of slope was considered as a rough boundary (following from Griffiths and Marquez (2007)). The geometry of the slope, and the initialisation of the soil slope in layers was the same as that used in the 2D plane-strain analysis, with a slice thickness of 30 m. The smooth boundary on one side was used to enforce symmetry in the problem; thus the slope analysed was 60 m wide, with rough boundaries on both ends.

The stresses were initialised in the soil with smooth boundaries on both sides. After the stresses were initialised, the displacements were reset and the boundary conditions modified such that one side was fully fixed. The strength reduction analysis was then initiated.

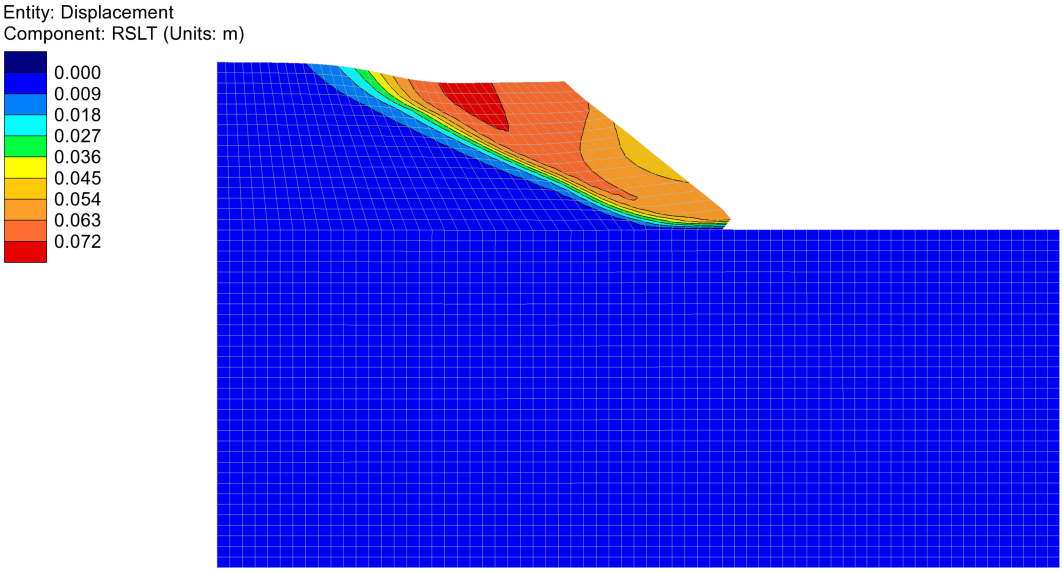

Figure 16. Resultant displacements for 2D plane-strain analysis at end of φ-c reduction, plotted at 20$\times$ exaggerated deformation.

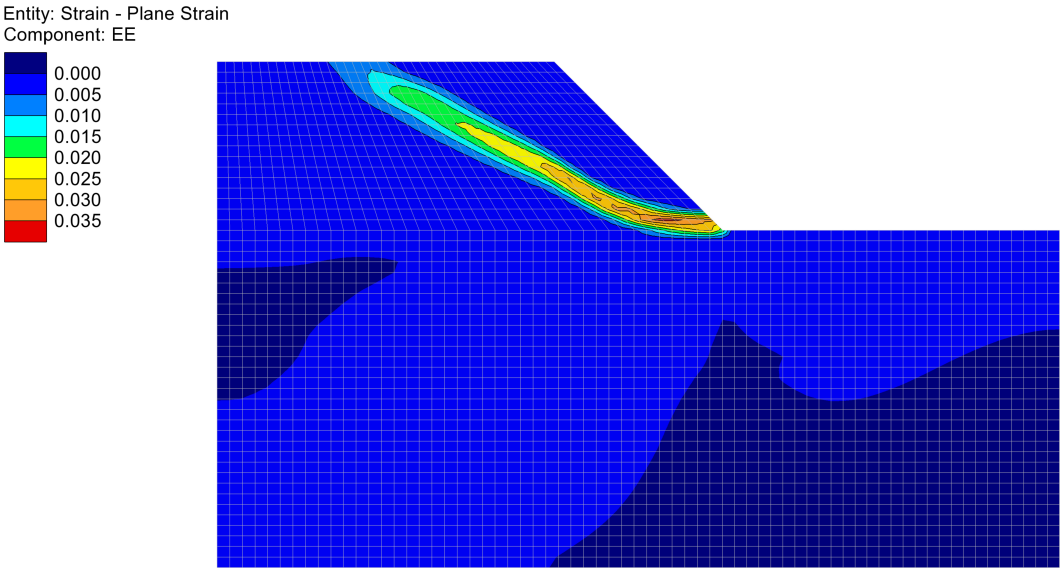

Figure 17. Shear strain for 2D plane-strain analysis at end of φ-c reduction.

The inclusion of the rough boundary has modified the nature of the failure in the slope. From the displacement plot (Figure 19), the shape of the failure surface is ellipsoidal. With the shear strain plot (Figure 20), the slip surface emerges at the toe of the slope near the smooth boundary.

The FOS calculated from the rough-smooth 3D analysis was 4.107. This is higher than the 2D plane-strain analysis which assumes smooth-smooth boundaries. This indicates that the rough boundary assumption increases the calculated FOS for slope analyses.

The automatic incrementation of the φ-c method in LUSAS means that many trial safety factors are used. Only those which converged are included in the output. The solution continues until the change in factor of safety is sufficiently small. In these analyses, this tolerance was set to 0.001.

For the gravity initialisation phase in the 2D slope, each increment required between 3 and 6 iterations to converge to the given tolerances (Figure 21). In the 3D analysis (Figure 22), the initialisation increments required 2 or 3 iterations. In both analyses,

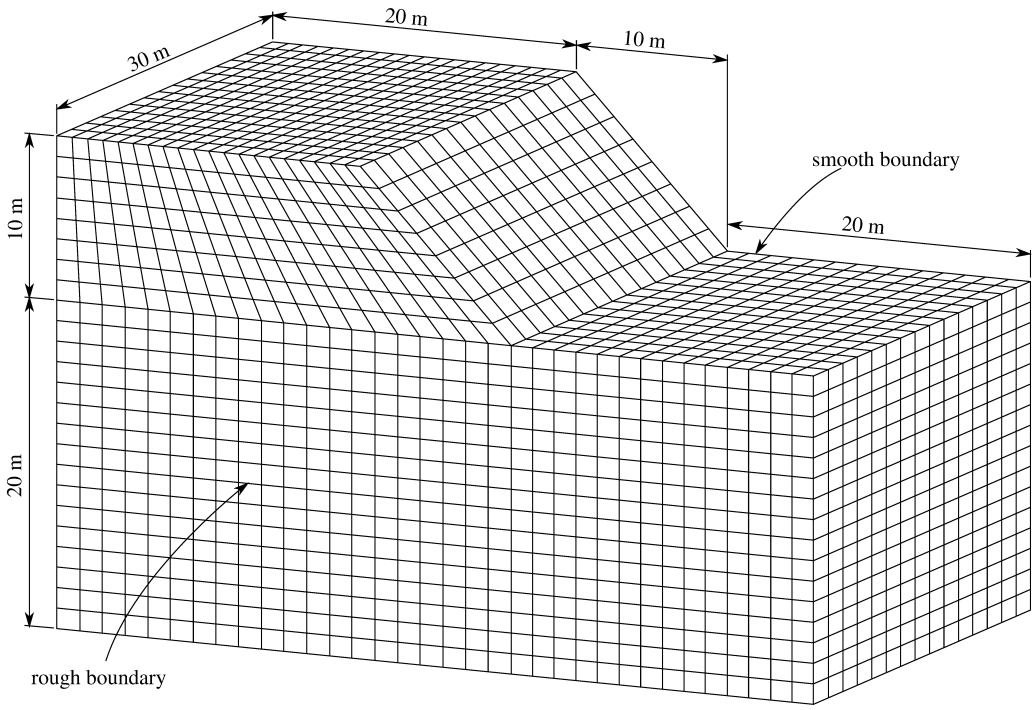

Figure 18. Mesh and geometry of the 3D slope stability problem. The base of the mesh is fully restrained, and the vertical sides of the mesh are restrained from deforming out of their respective planes; one of the vertical faces containing the slope is fixed in all directions.

The 4 lifts were performed using an automated incrementation procedure which increases and decreases depending on the number of global iterations required in the previous increment. Generally, each lift used between 8 and 10 incrementation steps for the 2D analysis, and between 4 and 6 incrementation steps for the 3D analysis. Between each lift, the calculated stresses were added to the equilibrium conditions and set as 'established' loads before the next lift was activated and gravity applied to it.

As the φ-c method initialised for both analyses, the global solution generally took between 5 and 13 iterations to converge. This increase in required iterations is to be expected as certain elements in the soil are being made to fail, and the degree of non-linearity is increased.

To demonstrate the rate of convergence of the HS-LC model, one increment from each of the slope analyses were chosen and the residual force norm (also known as the norm of the out of balance forces) are plotted for each chosen iteration. For the 2D plane-strain analysis, increment 44 was selected (Figure 23) and for the 3D analysis, increment 46 was selected (Figure 24). The finite element solution algorithm works to double precision floating point accuracy.

It may be seen from Figure 23 that, after the first few iterations, convergence progresses quadratically, and reaches a value in the order of 10^{-7} very quickly. The case is similar for increment 46 pf the 3D analysis (Figure 24) where the rate of convergence is initially in the order of 10^{-1} for a few iterations, and then accelerates dramatically to a value in the order of 10^{-11} by iteration 11.

The rapid rates of convergence, and the acceleration towards convergence shows that the implementation of the consistent tangent matrix in the HS-LC model works as expected, and the quadratic rate of convergence of the Newton-Raphson method has been preserved.

Finally, a mesh convergence study was performed for the 2D plane-strain slope (Figure 25). The original mesh consisted of 2,816 linear quadratic elements. A coarser mesh of 704 elements was generated by merging elements in groups of 4, and a finer mesh of 11,264 elements was generated by splitting each element into 4 equally sized smaller elements.

The variable compared in the mesh convergence study was the final FOS determined by the φ-c reduction method. The difference between the standard mesh and the coarse mesh is much greater than the difference between the standard mesh and the fine mesh.

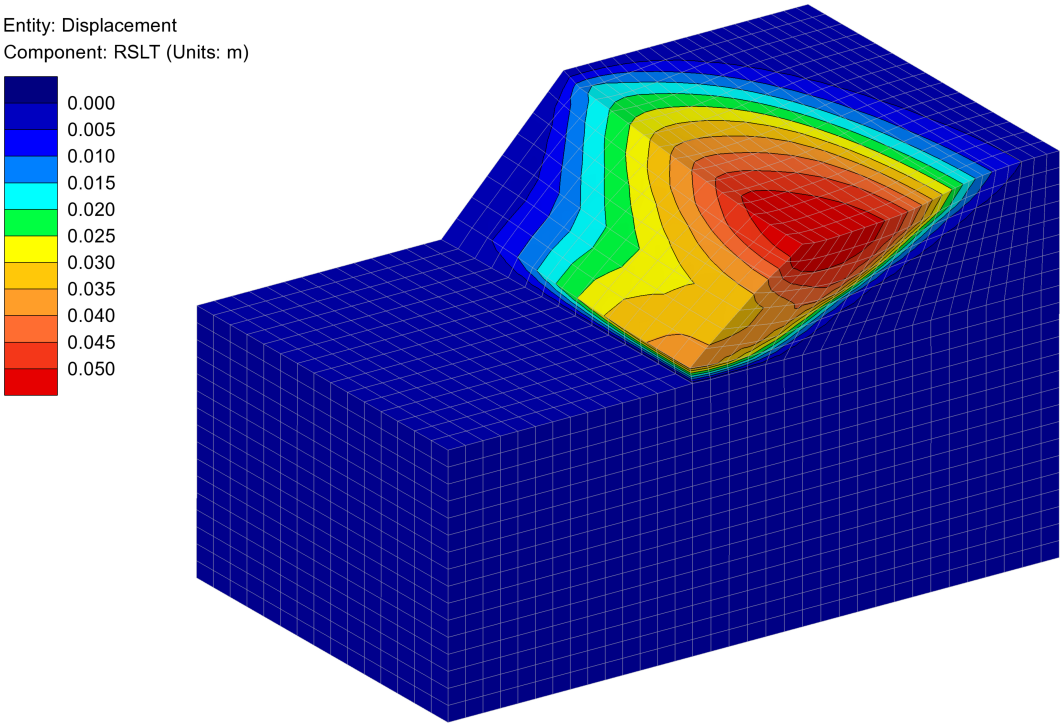

Figure 19. Resultant displacements for 3D rough-smooth boundary analysis at end of φ-c reduction, plotted at 40$\times$ exaggerated deformation.

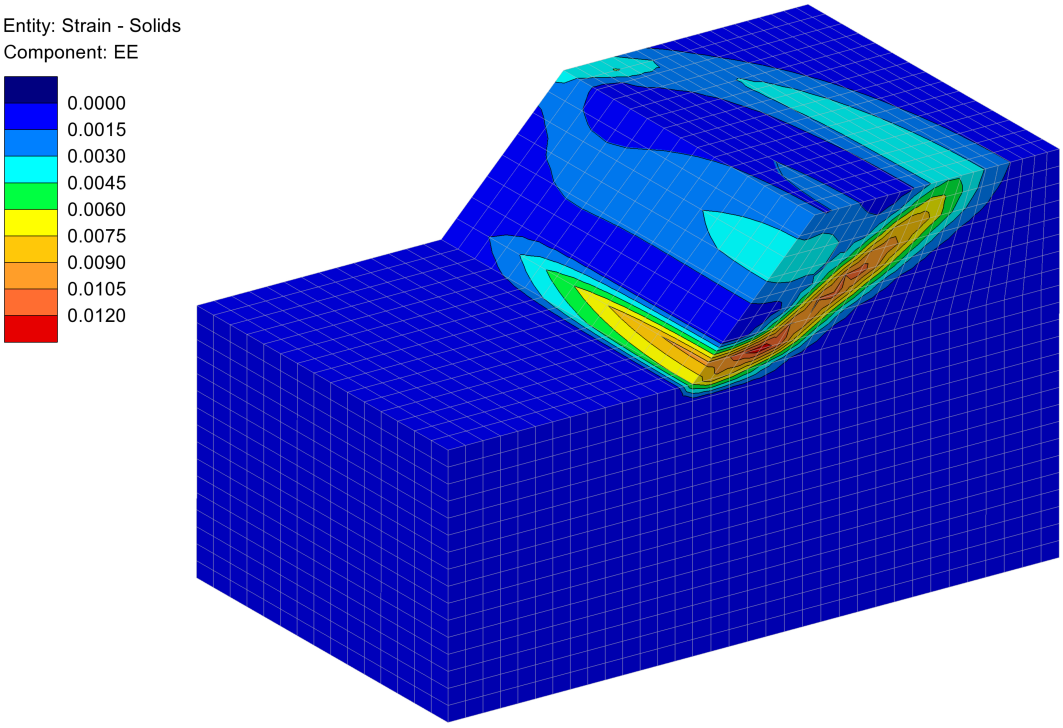

Figure 20. Shear strain for 3D rough-smooth boundary analysis at end of φ-c reduction.

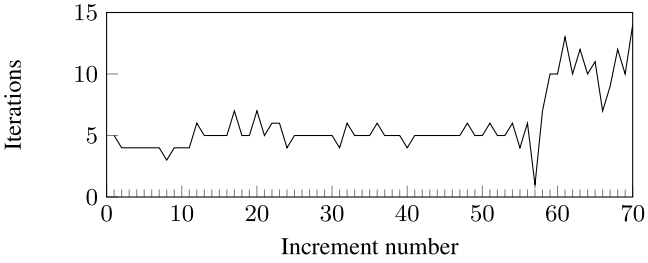

Figure 21. Number of iterations until convergence for 2D embankment analysis; increments 1-56 are the initialisation of gravity body forces in the slope, increment 57 is a displacement reset step, and the φ-c reduction method begins at increment 58.

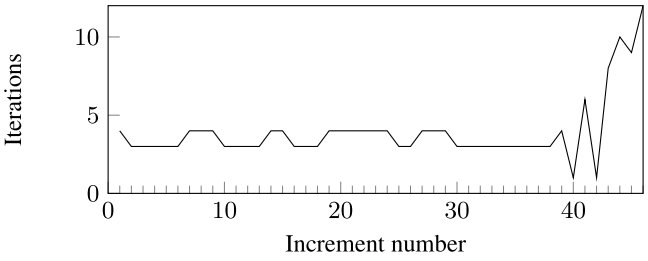

Figure 22. Number of iterations until convergence for 3D rough-smooth boundary embankment analysis; increments 1-39 are the initialisation of gravity body forces in the slope, increment 40 is a displacement reset step, the supports are modified at increment 41, a second displacement reset step is used at increment 42, and the φ-c reduction method begins at increment 43.

Therefore, it can reasonably be assumed that the mesh-converged solution for the FOS in this analysis is approximately 3.0.

The differences in the calculated FOS between mesh densities are likely to arise from the intersection of the slope and the base soil. This position is effectively a singularity, where a stress concentration can develop. The limitations of linear elements (i.e. shear locking) may also be contributing to some of the differences between meshes.

9. Conclusions

The implementation of the HS-LC model, with its new yield surface and hardening rule was able to reproduce results from the original HS model. The simulations using the new model were also a very good match for the laboratory based experimental results, following experimental curves very closely.

Several limitations were found with the previous version of the HS model, the first was the formulation of the shear yield surface,

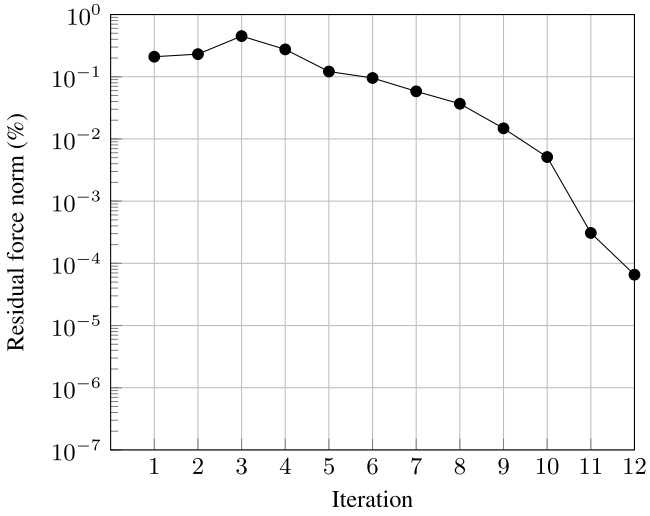

Figure 23. Residual force norm plot for increment 61 of the 2D plane-strain slope analysis.

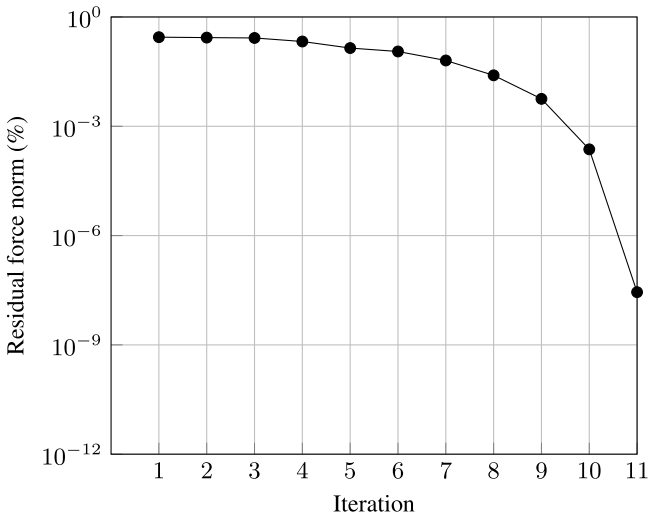

Figure 24. Residual force norm plot for increment 46 of the 3D rough-smooth slope analysis.

which produces an asymptote when the magnitude of the trial shear stress is too high. This was addressed by reformulating the shear yield function such that it remains positive for all shear stress above yield.

The previous versions of the HS model used incremental relationships and did not take the residuals of the state variables into account during stress return mapping. The new formulation presented here uses total relationships, and does include these residuals, consequently, convergence rates for these simple laboratory simulations were found to be very good.

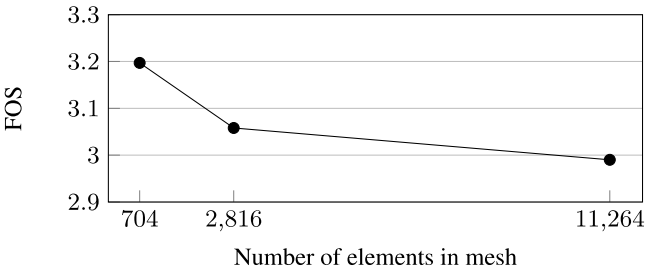

Figure 25. Mesh convergence plot of FOS for the 2D plane-strain analysis.

Use of a stiffness update procedure significantly reduced the amount of step size dependency in the HS-LC model, allowing use of larger step sizes without causing the solution to drift. However, this was found to come at a cost of marginally increasing the required number of iterations per increment. Use of the stiffness update procedure can be easily optimised to reduce the computational cost of analyses.

Applications of the HS-LC to boundary value problems were also tested with the analysis of a slope using φ-c reduction in 2D. The convergence of this analysis was stable, and the calculated factor of safety closely matched that calculated through analytical and graphical methods. A second slope stability analysis was also performed in 3D, with one of the boundaries considered as rough. This analysis predicted this factor of safety to be higher than the standard 2D plane-strain case.

Convergence rates for 2 particular iterations were also studied. The iterations chosen were at global soil failure and initially showed a slow and steady decrease in residual force norm, but the rate of convergence accelerated quickly as the iterations progressed; indicating that the quadratic rate of convergence of the Newton-Raphson method was preserved with the implementation of the consistent tangent matrix.

Acknowledgements

The authors would like to thank LUSAS and Innovate UK for funding this work under KTP project 9082. In addition, special thanks are also made to LUSAS for use of their software for this work.

REFERENCES

Benz, T. (2007), Small-strain stiffness of soils and its numerical consequences, PhD thesis, Universität Stuttgart, Institut für Geotechnik.

Benz, T., Wehnert, M. and Vermeer, P. A. (2008), A Lode angle dependent formulation of the hardening soil model, *in* 'Proceedings of the 12th International Conference of International Association for Computer Methods and Advances in Geomechanics', pp. 653–660.

Bower, T. A. (2017), Constitutive modelling of soils and fibre-reinforced soils, PhD thesis, Cardiff University.

Cocco, L. and Ruiz, M. (2018), Numerical implementation of hardening soil model, *in* 'Numerical Methods in Geotechnical Engineering IX, Volume 1: Proceedings of the 9th European Conference on Numerical Methods in Geotechnical Engineering (NUMGE 2018), June 25-27, 2018, Porto, Portugal', CRC Press, pp. 195–203.

Drucker, D. C., Prager, W. and Greenberg, H. T. (1952), 'Extended limit design theorems for continuous media', *Quarterly of Applied Mathematics* **9**(4), 381–389.

Duncan, J. M. and Chang, C. Y. (1970), 'Nonlinear analysis of stress and strain in soils', *Journal of the Soil Mechanics and Foundations Division* **96**(5), 1629–1653.

Griffiths, D. and Marquez, R. (2007), 'Three-dimensional slope stability analysis by elasto-plastic finite elements', *Géotechnique* **57**(6), 537–546.

Jiang, Z.-h. and Zhang, Y. X. (2012), 'Second development of hardening soil constitutive model in FLAC^{3d}', *Electronic Journal of Geotechnical Engineering* **17**(X), 3429–3439.

Lagioia, R. and Panteghini, A. (2014), 'The influence of the plastic potential on plane strain failure', *International Journal for Numerical and Analytical Methods in Geomechanics* **38**(8), 844–862.

Li, X. S. and Dafalias, Y. F. (2000), 'Dilatancy for cohesionless soils', *Géotechnique* **50**(4), 449–460.

Marcher, T. and Vermeer, P. A. (2001), Macromodelling of softening in non-cohesive soils, *in* P. A. Vermeer, W. Ehlers, H. Herrmann and E. Ramm, eds, 'Continuous and discontinuous modelling of cohesive-frictional materials', Vol. 568, Springer Science & Business Media.

Matsuoka, H. and Nakai, T. (1974), Stress-deformation and strength characteristics of soil under three different principal stresses, *in* 'Proceedings of the Japan Society of Civil Engineers', Vol. 9, pp. 59–70.

Obrzud, R. F. (2010), On the use of the hardening soil small strain model in geotechnical practice, *in* 'Numerics in Geotechnics and Structures', pp. 15–32.

Panteghini, A. and Lagioia, R. (2013), 'A fully convex reformulation of the original Matsuoka–Nakai failure criterion and its implicit numerically efficient integration algorithm', *International Journal for Numerical and Analytical Methods in Geomechanics* **38**(6), 593–614.

PLAXIS (2016), *Material Models Manual*.

Roscoe, K. H. and Burland, J. B. (1968), On the generalized stress-strain behaviour of wet clay, *in* 'Engineering plasticity', Cambridge University Press, Cambridge, pp. 535–609.

Rowe, P. W. (1962), 'The stress-dilatancy relation for static equilibrium of an assembly of particles in contact', *Proceedings of the Royal Society of London A: Mathematical, Physical and Engineering Sciences* **269**(1339), 500–527.

Schanz, T., Vermeer, P. A. and Bonnier, P. G. (1999), The hardening soil model: formulation and verification, *in* 'Beyond 2000 in Computational Geotechnics', Balkema, Rotterdam, The Netherlands, pp. 281–296.

Simo, J. C. and Hughes, T. J. R. (2006), Computational inelasticity, *in* 'Interdisciplinary Applied Mathematics', Vol. 7, Springer, New York, NY, USA.

Søreide, O. K. (1990), Mixed hardening models for frictional soils, PhD thesis, Norwegian University of Science and Technology, Trondheim, Norway.

Steward, T., Sivakugan, N., Shukla, S. and Das, B. (2010), 'Taylor's slope stability charts revisited', *International Journal of Geomechanics* **11**(4), 348–352.

Truty, A. and Obrzud, R. (2015), 'Improved formulation of the hardening soil model in the context of modeling the undrained behavior of cohesive soils', *Studia Geotechnica et Mechanica* **37**(2), 61–68.

Wehnert, M. (2006), Ein beitrag zur drainerten und undrainierten analyse in der geotechnik, PhD thesis, Universität Stuttgart, Institut für Geotechnik.

Wood, D. M. (1990), *Soil behaviour and critical state soil mechanics*, Cambridge University Press, Cambridge.

World Information Service on Energy (2014), 'Slope stability calculator', http://www.wise-uranium.org/csst.html. Accessed: 15/10/2018.